Design considerations for dynamic fluid flow in porous media experiments using X-ray computed micro tomography – A review

Tomography of Materials and Structures 3 (2023) 100017

Contents lists available at ScienceDirect

Tomography of Materials and Structures

journal homepage: www.journals.elsevier.com/tomography-of-materials-and-structures

Design considerations for dynamic fluid flow in porous media experiments using X-ray computed micro tomography – A review

Tannaz Pak [a,*,1], Nathaly Lopes Archilha [b,2], Steffen Berg [c,d,3], Ian B. Butler [e]

[a] School of Computing, Engineering & Digital Technologies, Teesside University, United Kingdom
[b] Brazilian Synchrotron Light Laboratory (LNLS), Brazilian Centre for Research in Energy and Materials (CNPEM), 13083-970 Campinas, Sao Paulo, Brazil
[c] Shell Global Solutions International B.V., Grasweg 31, 1031 HW Amsterdam, The Netherlands
[d] Department of Earth Science & Engineering, and Chemical Engineering, Imperial College London, United Kingdom
[e] School of Geosciences, The University of Edinburgh, Edinburgh EH9 3FE, United Kingdom

ARTICLE INFO

Keywords:
Fluid flow in porous media
X-ray computed micro tomography
X-ray transplant flow cell
Pore-scale imaging
Porous material
Fuel cell

ABSTRACT

Within the past decade, X-ray micro computed tomography (μCT) has become an advanced non-destructive tool to analyse the internal structure of opaque materials. In addition to high spatial resolution, new generations of laboratory-based μCT machines and synchrotron imaging facilities can achieve high temporal resolution. This makes μCT the method of choice to study dynamics processes such as multi-phase fluid flow within porous media at the micro-meter scale. To perform such experiments a system compatible with X-ray imaging is needed. This essentially includes an X-ray transparent flow cell which should both be compatible with the requirements of the experimental study and the constraints of the μCT facilities. So far, most μCT flow cells are custom built and optimised for specific experiments/purposes. This paper reviews the previously published X-ray transparent cell designs, their advantages, and limitations. We present the state-of-the-art in design of X-ray transparent flow systems and discuss the technical challenges around performing μCT-based fluid flow experiments. We also present a review of the main applications which have benefited from μCT imaging studies and discuss the flow cell designs according to applications.

1. Introduction

Advances in μCT data acquisition [1–4] and processing [5,6] techniques, specifically over the past decade, have enabled us to study the internal structure of opaque materials at micro and nano-meter scales. In addition to the study of sample structures under static conditions, μCT has become a common technique to investigate dynamic processes (i.e. where a change occurs over time) by collecting a sequence of 3D images as the process occurs and through comparing the image series both visually and quantitatively. A dynamic problem that has received significant attention is fluid (single or multiphase) flow in porous material (e.g. rocks and soil, fiber structures, technical ceramics) which are of great importance within the fields of environmental and energy engineering.

A conceptual experiment is sketched in Fig. 1. Experiments involve either laboratory-based μCT instruments or synchrotron beamlines. Both come with specific challenges and implications for the design of flow cell and flow infrastructure.

It is fair to say that the direct insight into microscopic details in particular access to the topology of the fluids within the pores and the time evolution in-situ/operando has led to unprecedented progress in the understanding of multiphase flow in porous media [1, 3, 7–19]. The following applications and problem fields have been the main driver for the development of μCT flow experiments: (1) Geo & Environmental Sciences (trapping efficiency in CO_2 sequestration [8,20,21], energy dissipation during immiscible displacement [15], complex displacement mechanisms in heterogeneous rocks such as carbonates [9, 11, 13, 22–27], hydrocarbon recovery such as improved recovery through low salinity waterflooding [24–27]), formation of gas hydrates in porous structures [28–31], formation of sea ice [32], drying and salt

* Corresponding author.
E-mail address: t.pak@tees.ac.uk (T. Pak).
[1] 0000-0001-7635-9333
[2] 0000-0003-0324-3748
[3] 0000-0003-2441-7719

https://doi.org/10.1016/j.tmater.2023.100017
Received 6 December 2022; Received in revised form 2 September 2023; Accepted 13 October 2023
Available online 16 October 2023

precipitation processes [33–36]), (2) Electrochemical/catalytical devices (limitations of transport in gas diffusion layers in fuel cells [37–39], shrinking and swelling of stack/assembly operando), (3) Materials Science (formation and (micro-) structure of metal foams [40], crumpled metallic foil meshes [41]), and (4) Food Science (stability of aerated products and emulsions, impact of freezing and thawing cycles on texture [42,43]).

The design and execution of experiments involving μCT imaging has evolved from a very challenging mode with relatively high failure rate to a (by now) more established process building on previous learnings and sufficient existing insights. Nevertheless, and perhaps because the information is scattered over a wide range of literature and sometimes only available in specific journals and communities, research teams still struggle with the design of such experiments. That is a problem in the sense that most of such experiments, at the frontier of research, are conducted at synchrotron beamlines. Access to beamlines is managed through a peer-reviewed process in which experiments need to be designed entirely upfront with very little room for testing in advance. In other words, if the experiment and respective equipment has not been properly designed, the beamtime itself can become less productive or a failure.

Typical challenges that such experiments face include:

- **Choice of material and the flow cell design** (e.g., sample size and wall thickness): This is particularly important for cases where higher pressures or elevated temperatures are studied. A compromise between mechanical strength and X-ray attenuation needs to be achieved. The complication is that the relationship between material choice, mechanical strength, required thickness and resulting X-ray attenuation are in some dimensions highly non-linear. For instance, the X-ray attenuation scales roughly with atomic number to the power 4–5 [44]. Thus, even though a stronger material may lead to a thinner wall and in principle reduce the X-ray attenuation, the strong scaling with atomic number may result in an ultimately higher attenuation. X-ray attenuation is X-ray energy-dependent, therefore it is important to understand the energy range available from the X-ray source. For benchtop instruments X-ray energy depends on the specifics of the X-ray tube, and for synchrotrons this is specific to the beamline. Generally, lower X-ray energies offer better contrast between different materials (e.g., different fluids) on the produced images. However, thick-walled flow cells made from high atomic number (high-Z) materials can significantly reduce the flux of low energy X-ray photons, when using a non-monochromatic X-ray source. This will adversely impact the signal-to-noise ratio and the quality of the produced image. For more discussions on image analysis the reader is referred to other review papers on this topic[1,3,6].
- **Destructive vs. non-destructive flow cells:** Relatively simple and easy-to-manufacture flow cells consist of hollow tubes of a rigid material such as carbon fibre epoxy into which the sample (and sometimes flow lines) are glued. These are destructive or single use because the sample cannot be recovered from the cell without damage and the flow cell cannot be reused. Non-destructive flow cells typically consist of a much more complicated design with e.g., sleeves that are pressed on the sample (using a confining fluid) to prevent bypassing of flow. These often require precision machining. The advantage is that the samples can be removed without damage and the flow cell can be reused.
- **Options for injection pumps and back pressure control:** Designs of flow cells with built-in micro pumps exist which reduces the dead volume (at the inlet) significantly. However, the back pressure control is challenging. External pumps, on the other hand, are more reliable, have larger volumes, but require long flow lines that need to be engineered in a flexible manner because the pumps are stationary while the flow cell must rotate during the X-ray imaging. This is a particular challenge faced in synchrotron experiments where continuous imaging is conducted to have the best possible time

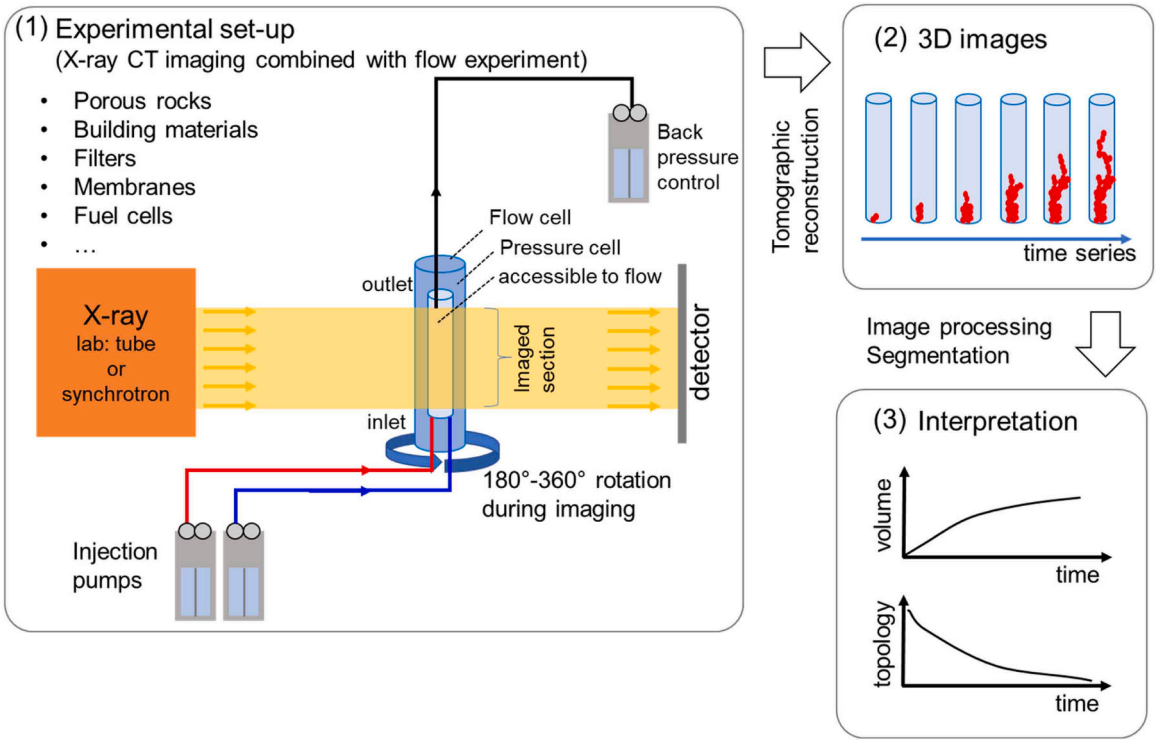

Fig. 1. Typical μCT flow experiment conducted in a flow cell with in-situ /operando μCT imaging. After tomographic reconstruction, a time series of 3D images is obtained, which are then further processed and analysed to obtain specific properties such as fluid saturation, topological or morphological descriptors vs. time. These then form the basis for theory development, validation of models, etc.

resolution. In contrast, some benchtop micro-CT instruments allow the flow cell to remain stationary which solves this issue.

- **The required resolution and field-of-view:** The field of view for μCT instruments is limited. Synchrotron beamlines operate in most cases with parallel beams of a beamline-specific maximum width and height. Because of the parallel beam geometry, there is less constraint on the wall thickness of the flow cell. Benchtop μCT instruments typically operate with a cone-beam geometry, where for a specific magnification or desired resolution there are very narrow constraints on the distance between the object and the X-ray source, which has implications for the maximum wall thickness of the flow cell.
- **Temporal resolution:** If high temporal resolution is required, fast rotation of the flow cell and short exposure times will need to be accommodated. This has significant implications for the design of the flow cell, the flow infrastructure, and the choice of construction materials for the flow cell.

Wettability alteration due to X-ray exposure is also a potentially relevant issue to consider, depending on fluids and materials [45]. In recent years, the μCT research community has introduced a range of designs for X-ray transparent flow cells to solve this compatibility issue. These include commercially available flow cells as well as custom-build ones, designed and constructed by different research groups. With the number of laboratory-based μCT instruments on the rise, μCT-based experiments are becoming a new routine in the field of material science, energy, and environmental engineering. Above all, porous media studies have benefited from these advancements. Therefore, we believe a review of the state-of-the-art in X-ray μCT compatible flow systems is of great assistance in facilitating future experimental designs.

Through exploring the designs previously proposed for X-ray transparent flow cells and discussion of their strengths and limitations we discuss the main challenges involved in conducting μCT-based fluid flow in porous media experiments. We highlight the challenges previously solved and the ones still outstanding.

While still not entirely standard, because the exact design depends on the exact scientific objective, we are now able to offer some general advice and guidelines for the design of an experiment involving μCT imaging and with respect to the flow cells and flow infrastructure.

The particular focus of this review is on flow cell design and selection of materials addressing the above-mentioned considerations and issues. In this paper we provide a review of successful designs of μCT-compatible flow cells, which are presented in an exemplary fashion by application. Applications range from geomaterials to electrochemical/catalytical devices (such as fuel cells) to materials and food science. We aim to summarise the learning achieved in a wide range of application domains. Each application has a specific scientific focus, and specific sample types, which have all significant impact on the design of the flow cell and flow infrastructure. For these reasons, this review paper does not offer a simple recipe that one just has to follow to arrive at the optimum design. When starting from scratch, the optimum design depends on multiple opposing factors and is typically an outcome of several iterations. The approach taken in this review paper is to present several designs that were successfully used for specific applications, which may serve as a good starting point for the design of the interested reader. Finally, we discuss a workflow that readers can use to build their flow cells either as a new design or by considering a previously established design. Using the learnings from this review paper the reader will be in a more informed position to make key design decisions according to the specific requirements of their experiment.

2. X-ray μCT imaging

X-ray μCT is based on taking a series of projection images from different angles which are then reconstructed to a 3D volume. For the projection images, X-ray photons produced using an X-ray source create a shadow of a sample (its projection) on a flat detector, as shown in Fig. 2. Through capturing hundreds to thousands of these projections through a full or partial rotation of the sample, a 3D volume (a 3D map of the X-ray attenuation coefficient in space) of the sample is obtained by applying tomographic reconstruction. The quality of the produced image depends on a number of factors including the specifics of the instruments used (e.g., the spot size and the energy range of the source and the physical pixel size of the detector), the sample size, and composition which will dictate the image resolution, sharpness, and contrast.

The situation in Fig. 2 represents attenuation contrast, which is the practically exclusive case for benchtop laboratory μCT instruments and also still very common for synchrotron beamlines. The contrast mechanism is based on the X-ray energy dependent X-ray attenuation, which is determined by a combination of material density and atomic number (more details will be given in Section 4.3).

Adding a doping agent can assist with achieving a better contrast between fluid and solid phases on the resulting images. The challenge here is to find a suitable doping agent and an optimum concentration for the doping agent selected to achieve the best image quality and importantly to avoid possible image artefacts that can be caused by excessive doping. Commonly used doing agents for the aqueous and organic phases in geoscience applications are potassium iodide and iododecane, respectively. Care needs to be taken to avoid unwanted reactions (such as corrosion) between these agents and flow cell components.

Synchrotron beamlines offer, in addition to attenuation contrast, also phase contrast, which is an interference effect for coherent X-rays which provides a contrast between e.g., different fluids without adding a contrast agent (which might be beneficial in cases where contrast agents alter the chemistry or other properties). At synchrotron beamlines this can provide significant contrast between materials that have only insignificant attenuation contrast. For laboratory instruments, phase contrast effects can lead to imaging artefacts. An overview of contrast mechanisms and beam geometries for benchtop μCT instruments and synchrotron beamlines is displayed in Table 1.

The design guidelines in this review paper are valid for both types of contrast. However, the discussion specific to the choice of materials in Section 4.3 is exclusively related to attenuation contrast.

3. μCT imaging in the laboratory and at synchrotron beamlines

X-ray μCT imaging is conducted using laboratory-based instruments or at synchrotron facilities. In selecting a suitable instrument for a μCT imaging experiment several factors need to be considered. These mainly include the sample size, the required spatial and temporal resolution, the material (to decide on the required X-ray energy), other components of the experimental set-up (e.g. environmental cells, injection pumps, compression/tension rigs, furnaces), required space around the sample, possible restriction to sample rotation during image acquisition, and possible adverse impact of X-ray exposure on other set-up components (more important in synchrotron-based experiments due to the high photon flux). For a review of laboratory-based μCT instrument components and design the reader is referred to Ruf and Steeb (2020)[46].

Synchrotron beamlines offer a significantly larger X-ray flux which allows faster image acquisition down to fractions of a second while benchtop instruments are limited to few minutes at a resolution of few micro-meters [1]. Also, the coherent and monochromatic X-rays offer specific contrast options which are not available using benchtop instruments. The main synchrotron facilities with μCT imaging beamlines are listed in Table 2. This table presents the available energy range, the sample size, and the achievable pixel size at the listed beamlines to allow direct comparison. A list of the web addresses (at the time of writing this manuscript) for these beamlines can be found in the Supplementary Information file, Table S1. It is worth noting that synchrotron facilities undergo planned upgrades every few years. For example, the Diamond

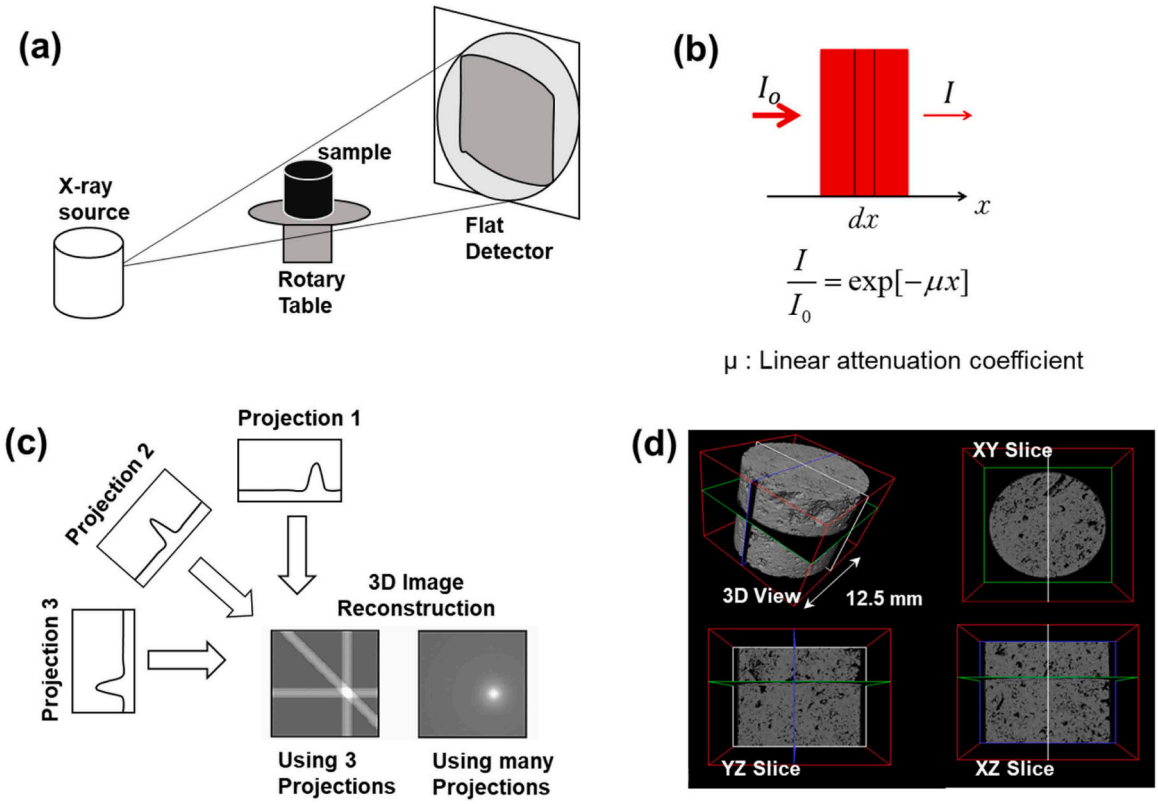

Fig. 2. (a) X-ray μCT imaging using cone-beam geometry showing the X-ray source, sample, and detector arrangement, (b) Beer-Lambert law which correlates X-ray beam intensity (I) reduction with the X-ray attenuation coefficient of the material (μ) and its thickness (x), (c) reconstruction of a 3D image based on 2D projections collected at different projection angles, (d) example of a 3D image of a rock sample with three slices through the image.

Table 1
Beam geometry and predominant contrast mechanisms.

	Parallel beam	Cone beam	Attenuation contrast	Phase contrast
Benchtop		X	X	
Synchrotron	X	(X)	X	X

Light Source is just about to start its upgrade, and the Swiss Light Source (SLS) started its upgrade in September 2023 and plans to be back online in 2025, while the European Synchrotron (ESRF) has already been upgraded to a new generation. Table 2 presents a summary of beamline characteristics at the time of writing this paper.

4. μCT imaging applications

The design of μCT-flow cells is largely driven by specific applications, which – via their respective specific requirements – largely influence or dictate the design of the flow cells. Therefore, in this section, the main applications for μCT imaging are briefly reviewed.

4.1. *μCT imaging for geoscience application*

μCT-based, in-situ, imaging of the dynamics of fluid flow in porous media has led to significant new findings, including (i) direct evidence that confirms a range of previously proposed pore-scale processes (e.g. Haines jumps [15,47,48], snap-off [13,15,49,50], trapping and ganglion dynamics in different flow regimes [8, 51–54], viscous fingering [48, 53], and capillary-end effect [52,55]) actually occur in 3D and within naturally occurring porous media, (ii) discovery of previously unrecognised mechanisms during immiscible fluid displacement (e.g. droplet fragmentation [13]), (iii) direct measurement of porous media wetting preference [56–61], (iv) evaluating/validating the outcomes of pore-scale models previously developed theoretically or based on observations within 2D flat capillary networks (micromodels) e.g. percolation theory [13,20], (v) discovery of the geometric state variables for capillarity which eliminate capillary pressure hysteresis [62], and (vi) proposing optimisation considerations/strategies for processes such as geological storage of CO_2, enhanced oil recovery [21, 53, 63–72], and subsurface storage of hydrogen [18,73,74].

μCT-based study of immiscible two-phase fluid displacement (e.g. oil/water or gas/water pairs) within artificial (e.g. sintered glass or bead packs) or naturally porous samples (mainly sandstone and carbonate rocks) has been conducted extensively in the recent years. However, imaging of three-phase fluid flow in porous media is significantly more complicated in terms of capturing the pore-scale dynamics. To date most three-phase studies have focused on providing insight into the distribution of gas/oil/water phases within porous media and detailing the main displacement mechanisms controlling the flow in such systems [71, 75–80].

μCT has been also applied to technologies such as low salinity water flooding (an enhanced oil recovery method) for which a wide range of underlying mechanism are proposed. μCT imaging has been used to understand the dominant controls responsible for the increase in oil recovery recorded in low salinity conditions. [11, 17, 24–27, 81–84]. Fluid-rock reactions within porous media have also been studied using μCT. The findings explain dissolution [85,86] and precipitation [35] reactions within porous media which are highly dependent upon fluid/rock composition and flow rates.

μCT imaging has been utilised to study the dynamics of water evaporation from saline porous media resulting in salt precipitation. The findings have informed the development of models to link the drying process to the main control parameters (such as porous media geometry) and to quantify the precipitation extent and pattern [33–35, 87].

Table 2
List of synchrotron facilities with μCT imaging beamline and their characteristics.

#	Light Source	Country	Beamline	Energy Range (keV)	Beam size (HxV) @ sample (mm^2)	Pixel size (μm)
Americas						
1	Advanced Light Source (ALS)	USA	8.3.2	6 – 43	40 × 4.6	0.45 – 9
2	Advanced Photon Source (APS)	USA	1-ID-B,C,E	42 – 140	2 × 2	1 – 2
3			2-BM-A, B	11–35	25 × 4	NA
4			5-BM-C	10 – 42	30 × 2	3 – 24
5			7-BM-B	5 – 150	10 × 4	NA
6			13-BM-D	10 – 100	50 × 4	NA
7			16-BM-D	20 – 30	0.5 × 0.5	1.3 – 2
8			32-ID-B,C	7 – 40	2 × 1	NA
9	Canadian Light Source (CLS)	Canada	BMIT	12.6–40	6.6 × 4	3.25
10	Brazilian Synchrotron Light Laboratory (LNLS)	Brazil	Mogno	22–67.5	0.075 × 0.075 to 85 × 85	0.050 to 55
Asia and Australia						
11	Australian Synchrotron (ANSTO)	Australia	Imaging and Medical	20 – 60	1.7 × 1.4 20 × 17 100 × 33	0.64 8 11.4
12	National Synchrotron Radiation Research Center (NSRRC)	Taiwan	BL01A1	> 4	19 × 9	20
13	Pohang Accelerator Laboratory (PAL)	South Korea	6 C	23 – 50	64 × 42 36 × 26.7 16.6 × 14 11.8 × 8.8	16 9 6.5 7.4
14	Photon Factory (PF)	Japan	BL-14 C	8 – 90	70 × 6	NA
15			AR-NE7A	22 – 55	80 × 3	NA
16	Synchrotron Light Research Institute (SLRI)	Thailand	BL1.2	5 – 15	8 × 4	1 – 5
17	Shangai Synchrotron Radiation Facility (SSRF)	China	BL13W1	8 – 72.5	12.1 × 12.1 7.6 × 7.6 3.8 × 3.8 1.52 × 1.52 0.76 × 0.76 0.38 × 0.38	5.9 3.7 1.9 0.74 0.37 0.19
Europe and Middle East						
18	Institute for Photon Science and Synchrotron Radiation (IPS)	Germany	Topo-Tomo	6 – 40	25 × 17 10 × 7 1.4 × 0.9	6.4 2.5 0.4
19	Diamond Light Source (Diamond)	UK	I12	50 – 150	46 × 12 20 × 12 8 × 7 3.3 × 2.8	18.5 7.9 3.2 1.3
20			I13	8 – 30	14 × 9.6 9.0 × 6.0 4.2 × 3.5	3.6 2.3 1.6
21	Elettra Synchrotron Trieste (Elettra)	Italy	Syrmep	8 – 35	4 × 4	1.95
22	European Synchrotron Radiation Facility (ESRF)	France	ID19	10 – 250	2.2 × 2.2 60 × 15	1.1 30
			ID17	25 – 185	95 × 7 60 × 7 16 × 7	47 30 8
			BM18	25 – 350	Up to 300	0.7 – 100
23	Deutsches Elektronen-Synchrotron DESY (Petra III)	Germany	PE05	5 – 50	7.2 × 7.2 3.6 × 3.6	2.4 1.2
24			P07	8 – 150	5 × 1	0.7
25	Bessy II	Germany	BAMline	8 – 60	9.2 × 7.8 3.7 × 3.1 1.8 × 1.5 0.92 × 0.78	3.6 1.44 0.72 0.36
26	Paul Scherrer Institute (PSI), Swiss Light Source (SLS)	Switzerland	Tomcat	8 – 45	13.3 × 11.2 8.3 × 7.0 4.3 × 3.5	5.2 3.3 1.6
27	Synchrotron SOLEIL	France	Psiché	15 – 100	16.8 × 5.9	NA
28	SESAME	Jordan	Beats	8 – 50	16.6 × 14.0 8.3 × 7.0 4.2 × 3.5 1.66 × 1.4	6.5 3.25 1.63 0.65
29 *	ALBA	Spain	Faxtor	8 – 70	35 × 12	0.5–10

* Beamline under construction and/or commissioning

Another application that has benefited from use of μCT imaging is study of the flow of colloidal suspensions in porous media [88–91]. Examples include the nano-remediation process that uses reactive nanoparticles (e.g. zero-valent iron nanoparticles) for in-situ remediation of contaminated groundwater through promoting degradation of the contaminant in place [14]. Similarly, injection of non-reactive nanoparticles has been studied using μCT imaging to inform nanotechnology-based enhanced oil recovery [22,92,93].

4.2. μCT imaging for fuel cells and electrochemical devices

Other applications that have advanced through μCT imaging of porous material include studies focused on the performance of fuel cells and batteries. Development of electrochemical devices has received considerable attention over the past decade. This is particularly important as we go through the energy transition by moving away from relying on fossil fuels and preparing to produce/store more renewable sources of energy at the industrial scale. μCT imaging is being used to investigate a range of mass transport phenomena in porous layers such as gas diffusion layers, membranes, and microstructures that are important components of electrochemical devices. The goal is to improve the performance and limit the ageing/degradation of these devices. For instance, hydrogen fuel cells produce water as a product of their chemical reactions that generate electricity. These cells consist of a gas diffusion layer and (depending on the type) a polymer membrane with a catalyst. The actual conversion occurs within the membrane which also is a proton charge carrier. For most operating types i.e., at elevated temperatures it is critical that this membrane is kept hydrated as the electro-catalytic reaction occurs in the aqueous phase. Therefore, in the gas diffusion layer, oxygen and hydrogen are dissolved from the gas phase into the aqueous electrolyte. To ensure the cell performance is optimised it is important to manage the simultaneous flow of gas and water through this gas diffusion layer [94]. At micro-scale water droplet formation, growth, and emergence of preferential flow pathways are controlled by the design of these porous layers, their surface wetting properties, and the capillary action [95]. Ultimately, the transport efficiency of gas and water in these membranes, i.e., the respective gas and liquid relative permeability, becomes the rate-limiting factor for the overall performance of these devices. Ex-situ microscopic imaging experiments performed using environmental-SEM and fluorescence microscopy have captured different water/gas transport behaviour for membranes with different structures and properties [96–100]. However, optimisation of the design critically depends on monitoring the actual gas and liquid distribution under *operando* conditions. In-situ 3D imaging of an operating electrochemical device offers clear advantages by providing direct visualisation and quantification means to study such dynamic mass transport processes in real time [37–39, 101–106]. For example, see the review by Bazylak (2009) [107] for a detailed discussion of the use of visualisation techniques in enhancing the design of PEM fuel cells.

Electro-catalytical CO_2 reduction has become an important topic within the context of decarbonisation and energy transition. CO_2 electrolysis is considered as a technology that can contribute to reducing CO_2 levels in the atmosphere while producing valuable chemical by-products such as carbon monoxide, formic acid, and alcohols [108, 109]. The techno-economic feasibility of CO_2 electrolysis at industrial scale is the key to making this technology a viable option [110]. In addition to scalability there are technical challenges at microscopic scale that need tackling [111–113]. For example, a specific limitation of this technology is bubble formation within the porous electrolyte layer and the gas diffusion layer (GDL) during cell operation. Identification of such micro-scale design limitations using X-ray μCT radiography has highlighted the need to devise improved GDL and porous membranes to enhance the performance of these devices [112].

3D imaging of the internal components of battery cells using X-ray μCT has also been subject of extensive research over the past decade. The focus is put on providing new and quantitative insights into the structure and material composition of batteries using this non-destructive technique. This is achieved by 3D imaging battery cells before, during, and after operation and cycling. Some of the key questions explored include understanding the impact of the electrode microstructure on cell performances or the influence of material heterogeneities on electrochemical responses. The reader is referred to the previously published research and review articles for more discussions on this subject [114–118].

4.3. μCT imaging for materials and food science

μCT imaging is applied to study in-situ processes involving fluid transport or phase transitions such as (i) formation of sea ice [32], (ii) formation of gas hydrates [28,30,31], (iii) aerated structures such as metal foams [40], (iv) emulsification within porous media [119], (v) solidification and crystallisation in metal alloys [120–123], and (vi) evaluation of the performance of new materials, for example self-healing concrete [124,125] and crumpled metallic foil meshes [41].

In the wider materials science space, which also includes applications in geosciences but also electrochemical devices, significant progress has been made to measure wetting properties and contact angle from μCT images [45, 57–59, 78]. The 3D imaging capabilities give access to mean and Gaussian curvature of liquid-liquid interfaces which has elevated the understanding of capillary equilibrium interfaces and wetting to an entirely new level [61,126]. The insight of very favourable two-phase flow hydraulic conductivity for bi-continuous interface configurations which was understood from research related to geomaterials [127] has opened the door for improved material design for gas diffusion layers fuel cells and other materials [127].

In food processing μCT imaging is used to analyse the structure of (e.g., aerated) food in 3D [43]. For example, the technique has captured the process of bubble formation and aeration [128]. Another example is the process of freezing and thawing of food and its impact on food quality which have been studied using μCT imaging [42,129].

5. X-ray transparent flow cells - design requirements/challenges

An essential part of a μCT-based 4D (time resolved 3D) imaging experiment is an X-ray transparent fluid flow cell (sample holder) that enables imaging of the sample and the fluids it contains, in-situ, without having to interrupt the sequence of experiment for the imaging purpose. That requires flow cells to be transparent for X-rays, which is not the case for conventional flow cells traditionally used in oil industry or hydrology laboratories. Such cells, for example Hassler type flow cells, are made of highly X-ray attenuating material, mostly steel, which enable experiments to be conducted at the high pressures and temperatures under which such flow processes occur in nature.

The main design parameters for X-ray transparent flow cells are (i) sample size considering the required resolution, (ii) material selection considering the operating conditions (e.g., temperature/pressure/reactive or corrosive fluids), (iii) compatibility with other components of the set-up, (iv) the dead-volume, and (v) establishing well-controlled boundary conditions. With respect to the selection of the structural materials used, the choice is significantly limited compared to conventional flow cells due to the requirement for the material to have a low or modest X-ray attenuation coefficient.

5.1. Sample size and effective image resolution

An important aspect of the flow cell design is the size because it impacts both resolution (in the field-of-view vs. resolution trade-off) but also the wall thickness (which scales nonlinearly with inner diameter). Therefore, sample size, and handling of respective samples, are important choices that influence the whole cell design.

Within geoscience applications, conventional flow experiments in porous media are conducted on samples (mostly cylindrical, cores or packed columns) typically of 25–38 mm diameter and 50–125 mm length. Subsurface geological formations of relevance (i.e., groundwater systems, hydrocarbon reservoirs, candidate formations for CO_2 or hydrogen storage) are either sandstones or carbonates. These rocks display pore sizes typically ranging from sub-μm to mm. Therefore, tomography images should be at least of μm-scale resolution to capture the details of such pore-systems. To achieve this with current μCT instrumentation, samples are required to be of only a few mm in size. The suitability of sample size should be discussed within the context of the

representative elementary volume (REV) for the porous media under study [130–132]. The REV of a rock is defined as the volume of the smallest samples of that rock for which the measured properties can be assigned to the entire system [133]. For homogeneous rocks, such as most sandstones, samples of a few mm size are typically representative, whereas more complicated structures that display features spanning several length scales require larger samples [134]. The trade-off between image resolution, sample size, and REV, therefore, is one of the primary considerations in designing a μCT-based experiment. This becomes less important when the studied sample is of homogeneous nature. A 5–10 mm diameter sample have been shown to successfully represent sand packs or homogeneous sandstones. Images of such small core plugs/columns typically achieve a few μm resolution which is commonly sufficient to understand the dynamics of the processes that take place within these samples. There are other μCT-based core flooding experiments reported in the literature where the sample under study displays heterogeneity. These studies have reported the use of larger samples. For instance, see Pak et. al (2015) [13,56] in which a 12.5 mm diameter core plug was used to ensure a REV for the carbonate rock under study (with pores spanning μm to mm sizes) was achieved. This is at the cost of coarser image resolutions. Other examples of imaging studies performed using larger samples can be found in the literature [135–137].

Apart from being representative, the main challenge in working with such small samples is their handling and preparation, specifically, when dealing with samples of lower mechanical strength such as poorly cemented grain stones, or highly porous rocks. Small core samples are typically drilled in a similar way to standard core plugs, i.e., using a drill press and small diameter drilling bits. At such small sizes any lateral movement during the drilling process can break the sample, making extraction of a sufficiently long core a difficult task. Such lateral movements can be caused by the drill bit (if skewed) or movements (vibration) in the rock during the drilling if it is not firmly held in place. To overcome the latter, supporting the sample structurally prior to cutting (coring) is a common practice. This is achieved by casting the sample in epoxy resin, plaster of Paris, or a similar casting material. To avoid penetration of the epoxy into the sample through the pores that touch the core wall a thin layer of epoxy can be applied to the outer boundary of the core prior to the casting process. Cryogenic drilling may also offer a solution, this method is practiced within the oil industry (at field scale) to stabilise boreholes that are pertinent to collapse by injecting nitrogen down the hole during drilling.

5.2. Material selection considering the operating conditions

When assessing materials for potential use in tomography flow cells, one starting point is to define the dimensions of the core to be used for the flow experiment, and the upper limit for pressure and temperature for the experiment. The sample dimension defines the inner diameter of any pressure vessel that might be required, and in combination with the maximum confining (or pore fluid) pressure it is possible to estimate the stresses exerted upon the most heavily loaded part of the pressure vessel wall. For a cylindrical pressure vessel, with end caps, containing a cylindrical sample plus a confining or pore fluid, the stresses on the vessel will be radial, axial and hoop stresses. The aim of vessel design is that the resultant stress should not approach the tensile yield stress of the pressure vessel material, nor overload the fasteners used to close the pressure vessel.

The additional constraint here is the requirement for a low X-ray attenuation property for the cell material (and its supporting components). This limits the range of suitable material to those with atomic numbers of 22 or less (based on authors' experience of the existing designs, and motivated on the one hand by the strong dependency of X-ray attenuation coefficient with atomic number that scales roughly as atomic number to the power of 4–5, but also the position of the K-edge in relation to the typical spectral range of the X-ray sources)[44]. Titanium (atomic number 22) can be employed in some synchrotron cells because it has still acceptable X-ray transmission (for energies above the K-edge) and excellent material strength. In selecting the cell material, the type of μCT instrument available to the study (i.e., laboratory-based instruments versus synchrotrons) also influences our choice. For example, synchrotron facilities provide significantly higher photon flux which allows achieving fast 3D tomography using titanium vessels, however, a titanium cell is not suitable for use with most laboratory-based instruments. Conversely, polymeric or resin components can be affected by the high X-ray flux at synchrotron laboratories, with potential (but uncertain) impacts upon mechanical performance.

Most of the X-ray transparent flow cells reported in the literature are made of (i) epoxy, (ii) carbon-fibre composites, (iii) polyether ether ketone (PEEK), (iv) polypropylene, (v) aluminium, (vi) titanium, and (vii) beryllium. Fig. 3 compares the linear X-ray attenuation coefficient (1/m) of these materials for a range of X-ray energies commonly used for tomography imaging. As shown the highest transparency is provided by polypropylene, epoxy, and PEEK, whereas aluminium displays a significantly higher X-ray attenuation. Note that the data shown here are for carbon fibre whereas in flow cells we use carbon fibre composites which are made of resin reinforced by carbon fibre. In using such composite material, the X-ray beam path length through the carbon fibre is commonly 20–30% (or less) of the wall thickness. Therefore, the carbon fibre tubes used in flow cells are significantly more X-ray transparent when compared with aluminium.

Effective X-ray attenuation coefficients of materials consisting of multiple chemical elements can be computed more efficiently using spreadsheet-based tools such as MuCalc [139].

A flow cell needs to accommodate the required operating conditions specific to the dynamic process under study. Based on the actual designs used in practice (Table 3) we find two common principles for the selection of the core holder material are.

- Temperature range
- Pressure range

and a combination thereof. For study of flow processes within shallow groundwater resources modest P/T ranges ($P < 1$ MPa and $T < 50$ °C) are sufficiently representative. However, within deeper geological formations flow occurs under much higher P/T (P in range of tens of MPa and T in range of hundreds °C). Performing experiments at such elevated P/T conditions provides a more realistic picture of relevant flow processes, specifically, considering that some of the key fluid properties are P/T dependent, e.g., fluid-fluid interaction (e.g., miscibility), fluid volumes (compressibility), fluid viscosity and density (specifically for the gas phase). In addition, some processes can only be studied within a specific range of P/T, for instance, where one of the phases forms under specific conditions e.g., $scCO_2$ or gas hydrates.

To account for the structural integrity of flow cells the main factor to consider is the material properties e.g. mechanical strength/thermal tolerance of the components of the flow cell. Mechanical data for engineering materials may be provided by the supplier or obtained from resources such as Matweb (an online material property database) [140]. Detailed information on how properties may vary subject to temperature, and duration of exposure to temperature are detailed in texts such as [141]. For many experimental applications related to fluid flow, it is sufficient to note the yield strength for materials at ambient temperature or close to it. However, increasing temperature may place design constraints upon materials, and it should be noted that as temperatures increase above 100–150 °C, both metals and engineering polymers may start to show significant deviations from their ambient temperature yield strength. PEEK passes its glass transition at 143 °C, with consequent reduction in strength, and many aluminium alloys begin to show significant reduction in both yield and ultimate tensile strength above 150 °C. Furthermore, the duration of exposure to elevated temperature is an important consideration and extended (hundreds to thousands of

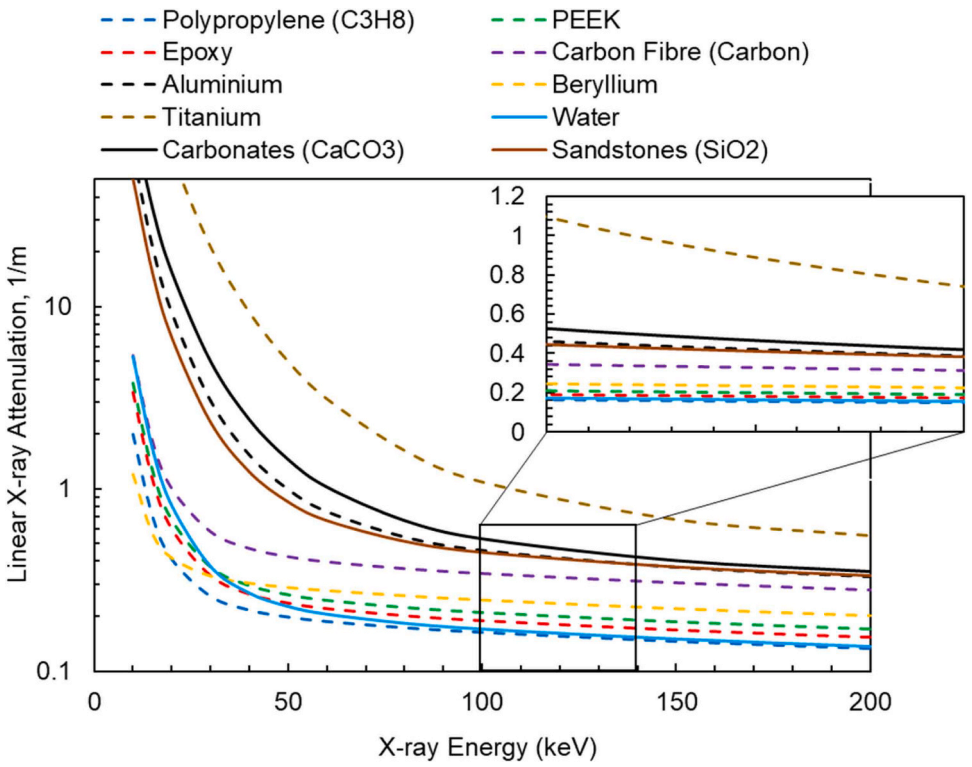

Fig. 3. Comparison of the linear X-ray attenuation coefficient for a range of commonly used flow cell material, also plotted is the attenuation of water, calcite, and quartz. The data are extracted from the XCOM data base[138].

hours) exposure to temperatures in excess of 100 °C can significantly reduce the yield and ultimate tensile strength of alloys such as 6061-T6 and 7075-T6 aluminium [142]. The effect of temperature is particularly marked for alloys from the 7000 series which, at ambient temperature, offer excellent mechanical strength far beyond that offered by other aluminium series, but which degrade quickly at temperature. Alternative materials exist for materials to make pressure vessels if elevated P and T are required. Grade 5 Titanium alloy offers excellent strength and can be used beyond 200 °C but is more attenuating than aluminium and may be restricted to applications where high X-ray fluxes are available. Alternatively, magnesium alloys such as Elektron® 43 offer low density (1.8 g.cm^{-3}) and good mechanical properties to temperatures up to 300 °C. While we are currently unaware of any applications using these alloys, in the Edinburgh Experimental Geoscience laboratories, we have started to integrate such materials into our flow cell Mjolnir [143] with promising indications, especially with regards to X-ray transparency. Such materials, however, are incompatible with water or other aqueous solutions during use.

For most experimental flow applications, lightweight, easily obtained engineering materials such as PEEK and aluminium have proven to be excellent for the construction of X-ray transparent pressure vessels. It is the introduction of elevated temperature above 100 °C that can introduce more complex considerations in pressure vessel design. In such circumstances it is essential to stick to good practice and to ensure that the stresses at maximum operating pressure and temperature are well inside the limits of the material strength. Furthermore testing, with or without independent certification, of the vessels is essential prior to using the vessels in an experimental assembly.

In addition to the above discussions, the mechanical properties of respective materials dictate how respective cells can be manufactured and used. For example, a machinable material such as aluminium can be used for all components of the cell if non-aggressive (e.g., non aqueous fluids) are studied. Another example is that combining epoxy and carbon fibre composite with other materials is a challenge as they cannot be fitted with threads and the other mechanical elements required to join components of the cell together.

Another consideration for material selection is the manufacturing limitations associated with them. Among the materials discussed above, carbon fibre, being a fibrous material, is typically spun. Postprocessing by machining is only possible to a limited extent without compromising its strength. End flanges for instance need to be either glued or clamped. Challenging production of adequately smooth surfaces with conventional cutting routines has resulted in development of controlled techniques with specific tools and cutting conditions [144] suitable for machining carbon fibre.

Beryllium and its composites are known to be toxic and carcinogenic presenting risks/limitations on working with them. For instance, debris generated during machining beryllium parts are strictly regulated to limit worker's exposure [145].

The end pieces can be made of any material (commonly made from stainless steel) since these are not within the imaging field of view. However, considerations around selecting materials for end pieces come from the way the flow cell is designed and assembled and the possible impact having a heavy (e.g., metallic) end piece may have on introducing movements because of rotation during imaging. Where flow cell body is made of flexible material lighter end pieces can reduce the probability of movements during imaging (which can result in blurred images). [138,144,145].

5.3. *The seal, flow lines and connectors*

To prevent leakage of fluids a flow cell needs to be sealed. Typically, the seal is achieved using mechanical gaskets (O-rings) that are placed between the components of the flow cell (e.g., the body and the end pieces) filling designated seal grooves. O-rings are made of a range of materials. A low cost and commonly used O-ring material is nitrile butadiene rubber (NBR) which is suitable for low temperature applications (below 100 °C). Viton rubbers are suitable for application at higher temperatures (above 100 °C). Both NBR and Viton are not suitable for experiments involving super-critical CO_2 ($scCO_2$).

Table 3
Design characteristics for X-ray transparent core holders used in previous studies.

	Authors/ Publication year	Material / Design specifications	Pressure / Temperature Range	Sample size / Special Feature	CT Scanner / Synchrotron facility used with this cell
1	Bazin et al. (1996) [162]	Plexiglass	Low / T = 50 °C	D = 50 mm, L= 50–200 mm Chemical Resistance to HCl acid	Fourth-generation medical CT
2	Coles et al. (1998) [163]	• Bio-plastic® body (a liquid casting plastic) • Plastic end pieces Core wrapped with Teflon® tape, plastic flow cell created by moulding in place, around the plug and end pieces, cured for 48 h.	Low / ambient	D = 25.4 mm L= 31.8 mm Larger sample size	Brookhaven National Laboratories
3	Schembre and Kovscek, (2003) [164]	• Body made of acrylic tubes.	< 1 MPa / ambient	D = 24 mm, L= 88 mm	Desktop
4	Viggiani et al. (2004) [165]	• Body made of Plexiglass (5 mm thick) Core placed in a thin latex sleeve	1 MPa/ ambient	D = 20 mm, L= 40 mm This is a triaxial cell that allows triaxial compression of samples.	ID15 at the European Synchrotron Radiation Facility (ESRF)
	Schnaar and Brusseau, (2005) [166]	• Aluminium body • Stainless steel end fittings Designed to hold sand/bead grains, uses porous frits (polypropylene/stainless steel) at both ends of the column to retain particles.	-	ID = 4.6 mm or 5.8 mm, L= 44 mm	Advanced Photon Source (APS), Argonne National Laboratory
5	Du et al. (2008) [72]	• PEEK body Core encapsulated in a 2 mm thin layer of low X-ray attenuating Araldite (CW 2215) glue with the CIBA HY 5160 as hardener.	0.5–1.75 MPa / ambient	D = 48 mm, L= 220 mm	Third-generation medical CT
7	Iglauer et al. (2011) [69]	• Carbon fibre body • Stainless steel end pieces • Viton sleeve Core wrapped in thin aluminium foil (50 μm thick) to prevent $scCO_2$ from escaping the Viton sleeve	Pore = 9 MPa Confining= 11.75 MPa T = 50 °C	D = 4.95 mm L= 9 mm Designed to be used with super critical CO_2	Desktop Later used at Diamond Light Source
8	Armstrong et al. (2012) [7]	• Glass chromatography column packed with glass beads A semi-permeable, hydrophilic membrane was placed at the bottom of the column to prevent the organic fluid to escape the column.	Pore < 1 MPa / ambient	ID = 3.5 mm, OD = 7 mm L= 25 mm	Advanced Photon Source (APS), Argonne National Laboratory
9	Zuo et al. (2012) [65]	• Body made of polyamidimid (high-tensile-strength plastic) cylinder with ID= 50 mm, OD= 100 mm The two ends of the core holder are wrapped with a cloth heat tape for temperature control.	10 MPa/ 40 °C	D = 35 mm, L= 70 mm Specially designed for studying super critical CO_2	Medical CT
10	Zuo et al. (2012) [65]	• Aluminium body Triple wrapped in (i) heat-shrinkable Teflon sleeve, (ii) nickel foil (to prevent diffusion of CO_2 through the confining Viton sleeve) and (iii) a Teflon sleeve.	2.75–12.41 MPa / 50 °C	D = 50 mm Specially designed for studying super critical CO_2	Desktop
11	Alemu et al. (2013) [70]	• Composite structure of steel and carbon-fibre • Nitrile • Rubber sleeve	10–30 MPa / ambient	D = 38 mm, L= 100 mm Coupled resistivity measurements along the axis of the rock	Desktop
12	Berg et al. (2013) [15]	• Polycarbonate cylinder • Heat-shrink on rock sample (no sleeve).		D = 4 mm, L= 10 mm A micro–piston pump integrated into the sample holder	TOMCAT beamline at the Swiss Light Source
13	Akbarabadi and Piri, (2013) [64]	• Aluminium body Core and sleeve wrapped with several layers of aluminium foil and Teflon tape to prevent CO_2 penetration through the sleeve and ultimately into the overburden fluid.	11 MPa/ 55 °C	D = 38 mm, L= ~150 mm Specially designed for studying super critical CO_2	Medical CT
14	Pak et al. (2013) [56]	• Epoxy resin encased core • Delrin® (Polyoxymethylene) end pieces • Nylon threaded rods located through two aluminium plates	0.7 MPa/50 °C	D = 12.5 mm, L = 44 mm. This design can accommodate smaller diameter and longer cores too.	Desktop
15	Fusseis et al. (2014) [167]	Modular cell. Depending on the required X-ray transparency the body can be made of: • Aluminium • Stainless steel tube stubs • Carbon fibre	Confining 20 MPa, Pore 15 MPa / 200 °C	D = 3 mm L= flexible, Useful for X-ray flux density of 10^9 photons mm^{-2} s^{-1} and energy range 30–100 keV	2-BM beamline at the Advanced Photon Source (APS)

(*continued on next page*)

Table 3 (*continued*)

	Authors/ Publication year	Material / Design specifications	Pressure / Temperature Range	Sample size / Special Feature	CT Scanner / Synchrotron facility used with this cell
		The core is encased in jackets of elastic silicone and high-temperature heat shrink tubes. The cell is heated by two band heaters mounted around the upper and lower endcaps. This cell is available to all users at the APS.			
16	Lebedev et al. (2014) [168]	• PEEK body	Confining 8 MPa, Pore 6.5 MPa / 45 °C	D = 38 mm, L= 80 mm Simultaneous acquisition of acoustic and CT data	Desktop
17	Tisato et al. (2015) [169]	• Body made of aluminium alloy (7075-T6)	Confining 20 MPa / ambient	D = 12 mm, L= 36 mm Designed to measure seismic wave attenuation	Desktop
18	Chaouachi et al. (2015) [29]	• Aluminium sample holder The holder mounted onto an aluminium cylinder, sealed with a transparent polyethenimide dome.	0.1 <P < 0.6 MPa / 3 °C	D = 2 mm, L= 10 mm Specially designed for studying hydrate formation	TOMCAT beamline of the Swiss Light Source
19	Herring et al. (2016) [68]	• Titanium core holder manufactured at the Australian National University (wall thickness of 0.12 mm) Core wrapped in Teflon tape and inserted into the core holder onto a circular hydrophilic nylon membrane with pore size of 1.2 μm	- / ambient	D = 4.9 mm, L= 8.5–10 mm	Desktop
20	Dobson et al. (2016) [170]	• Perspex or aluminium tube (1 mm)	Adjustable to high P / T with Aluminium body	D = 6–25 mm Variable volume flow cell, mounted outflow reservoir inlet tube attached to the top of the cell	JEEP i12 beamline, Diamond Light Source
21	Jervis et al. (2016) [171]	• Polypropylene tube • Aluminium spacer disks • Carbon felts • Viton O-rings • PTFE ring gaskets	Low / ambient	D = 11 mm Chemical Resistance to 3 M sulphuric acid	TOMCAT beamline of the Swiss Light Source synchrotron
22	Bultreys et al. (2016) [153]	• Body made of poly-methyl-methacrylate (PMMA), low-cost thermoplastic Core wrapped in put in a Viton sleeve	Low pressure / ambient	D = 6 mm, L= 17 mm	Desktop
23	Renard et al. (2016) [155]	• Body is machined in a single piece of titanium with wall thickness of 5 mm The core is encased in a Viton rubber sleeve, (1.5 mm thick), to ensures a perfect sealing between the confining fluid and the sample.	Confining P to 100 MPa, axial stress to 200 MPa, temperature to 250 °C	D = 5 mm L = 10 mm Triaxial deformation apparatus Transparent to high-energy X-rays above 60 KeV	HADES Cell at beamline ID19 of the European Radiation Synchrotron Facility (ESRF)
24	Lebedev et al. (2017) [63]	• PEEK body (ID= 8 mm, OD =21 mm, L=300 mm) Core placed in a rubber sleeve and was connected to the fluid lines using custom made plastic end pieces.	Confining 20 MPa/ Pore 10 MPa / up to 80 °C	D = 5 mm Specially designed for studying super critical CO_2	Desktop
25	Dalton et al. (2018) [172]	• Beryllium core holder Cores were placed in a confining sleeve with aluminium spacers at both ends to eliminate capillary end effects	Confining 14.5 MPa / Pore 12.4 MPa / temperature to achieve scCO2 conditions (47.0 °C)	D= 6.35 mm L= 40.64 mm Used with super critical CO_2	Desktop
26	Øren et al. (2019) [173]	• Aviation grade aluminium alloy (T7000 series) High pressure, high temperature triaxial flow cell capable of withstanding radial and axial pressures of up to 69 MPa Cores were encased in shrink-wrap, flow lines were semi-permanently installed and connect to the cell through the base of the rotational/translational stage, alleviating issues with rotation	Pore 1 MPa, ambient temperature	D= 12 mm L= 40 mm	Desktop
27	Butler et al. (2020) [143]	• Al alloy and Ti cell. • Core is encased in a Tygon sleeve (1.6 mm thick) and held between two Ti-tipped pistons. The originally published design has been further adapted to accommodate fluid flow	Confining to 50 MPa/ Pore to 40 MPa/ Axial stress to 670 MPa/ up to 140 °C	D = 3.2 mm L = < 20 mm Triaxial deformation apparatus with fluid flow capability transparent above 20–30 keV.	TOMCAT SLS JEEP I12, DLS PSICHE, SOLEIL 2BM APS
28	Thaysen et al. (2022) [18]	• Carbon fibre loaded PEEK cell with 316 stainless steel end caps. • Core wrapped in Al foil and sealed with heatshrink/silicone. Designed for use with H_2/ brine flow experiments.	Confining to 15 MPa/ Pore to 12 MPa. Ambient temperature	D = 5 mm L < 50 mm	Desktop JEEP I12 DLS

Perfluoroelastomers (FFKM) are copolymers of tetrafluoroethene and a perfluorinated ether such as perfluoromethylvinylether. A range of formulations of FFKM exist for O-ring applications offering both excellent chemical resistance and temperature resistance beyond 250–300 °C. Their limitation is their significantly higher cost over other O-ring materials. Polytetrafluoroethene (PTFE) O-rings offer excellent chemical resistance and can be used up to 240 °C but are not elastomeric and so are restricted to static applications and cannot be reused.

To connect the components of the flow system three main types of fittings are commonly used in μCT-based flow set-ups, these are: (i) Low

pressure liquid chromatography (LPLC) fittings, (ii) high performance liquid chromatography (HPLC) fittings, and (iii) Swagelok fittings. LPLC fittings may be made from a range of polymers including PEEK, ETFE (Ethene tetrafluoroethene), Delrin (Polyoxymethene), and PFA (Perfluoroalkoxy alkanes). Maximum working pressures for LPLC fittings are subject to the material and tubing size but some can extend up to 13.8 MPa, making them useful for many fluid flow applications. HPLC fittings may be made from PEEK or stainless steel, and maximum operating pressures extend from 30 MPa to over 200 MPa, making them suitable for investigations of flow under deep reservoir conditions. Swagelok provides a versatile selection of fittings, adapters and valves principally in 316 stainless steel but also in materials such as Alloy 400 (Monel) and Alloy C-276 (Hastelloy) and PTFE, which may find applications in experiments involving aggressive fluids. All the fittings mentioned are compatible with flexible tubing and HPLC and Swagelok are also compatible with stainless steel tubing to provide excellent leak-free connections. The experience of the University of Edinburgh laboratories is that for elevated pressure experiments which require the flow cell on the rotary table to be connected to static pumps positioned away from the rotary table, it is useful to use a combination of fittings and tubing types. PEEK tubing is used to provide the flexibility required to accommodate rotation, while stainless steel tubing permits tighter turn radii often required when attaching fluid inlet tubing to the experimental cell. In all cases, flexible tubing must be strain relieved by attaching it firmly to the rotary table so that there is no flexural force applied to the unions joining the fluid inlet and outlet tubing to the cell itself.

In terms of tubing, where possible, transparent tubing is the preferred option to allow visual monitoring of the injected fluids. This is specifically useful for (i) detecting/avoiding injection of unwanted fluid phases, e.g., air bubbles, and (ii) to decide on the onset of high frequency imaging (the injected fluid reaches the sample inlet), useful for real-time 4D experiments. Experiments at significantly elevated pressures preclude the use of transparent tubing.

5.4. Injection system, pumps, and back pressure

Many experiments are designed to operate at injection rates representative of subsurface reservoirs, corresponding to a flow velocity of 1 foot / day or capillary numbers (Ca) of the order of 10^{-6} or lower. Ca is defined as the ratio of viscous to interfacial forces. This poses a particular challenge to injection pumps to deliver this flow rate continuously and without any pulses. While pumps operated with linear electric motors do not exhibit such steps, pumps driven by stepping motors can potentially exhibit pulses. Special attention needs to be paid to the injection rate associated with a single stepping motor step. A pump driven by a stepping motor is not necessarily a showstopper because gear systems can still translate those steps into miniscule flow rates or capillary numbers for each pulse that are individually smaller than Ca$\sim 10^{-6}$. But pumps with large piston diameters could potentially lead to larger steps, which would then lead to an overall pulsating flow and consequently artefacts in the experiment.

Pulsation can also be caused by stick-slip motion of the plunger when using syringe pumps at lower pressures and is not exclusively connected to stepping motors, although the biggest risk is probably the discontinuous pumping of pulsating stepper motors at low flow rates.

Another potential source of pulsations is the bending of flow lines during the 180–360 degrees rotation of the core holder on the rotation stage while performing tomography. PEEK capillaries may appear as rigid but nevertheless, bending can lead to – depending on pore pressure and pore volume – potentially significant flow. It is difficult to predict the significance of this effect because it depends on various factors. It is therefore better to check, ideally with a pressure transducer, how much pressure fluctuations are generated when rotating the core holder with attached flow lines. Additionally using wide turn radii and narrow bore PEEK tubing helps to further alleviate this potentially significant problem.

These considerations lead to overall two main design concepts. One is to integrate the injection pumps into the core holder [15,16] and the second is to have the pumps outside the cell. In the former design, custom-designed pumps were used which operated with linear motors normally used to align mirrors on optical tables (e.g., Physik Instrumente). To achieve lower flow rates, the attached gear box was replaced by one with a lower gear ratio (Faulhaber). The great advantage of this design concept is that the injection is really pulse-free, and the dead volume is very small. Also, no flow lines or cables need to be attached. Electrical power to the motor control systems can be provided by the slip rings, and general control and data transfer of pressure measurements can be realised by a wireless data transfer system. The disadvantage of this design is that back pressure is just atmospheric pressure. Due to limitations in weight and design height, it is very difficult to have a similar pressure control system at the outlet, therefore, these experiments were typically operated without back pressure control, i.e., operated with a back pressure being just atmospheric pressure. Therefore, the pore pressure is in most cases also practically atmospheric, which makes it very difficult to suppress the formation of gas bubbles due to exposure of the fluids to X-ray photons which is a challenge faced at synchrotron laboratories while imaging using low energy pink beam. The bubble formation issue is suppressed when monochromatic beam is used at higher energy levels.

It is also known that a back pressure of 0.5–1 MPa will largely prevent the formation of gas bubbles. However, that requires an entirely different design concept with high-pressure injection pumps (e.g., ISCO or Cetoni) and similar pumps used for back pressure control. These pumps typically exceed size and weight of the rotation stage and therefore need to be placed outside of the rotation stage, connected to the rotating column (core holder) with flexible flow lines. Such designs can easily realise pressures over 10 MPa e.g., for supercritical CO_2 experiments.

Multiphase flow experiments typically require more than one pump. Ideally, core holders are designed such that the e.g., two injection lines meet only inside the core holder at a distribution manifold which consists of a system of grooves followed by a porous injection disk made e.g., out of a ceramic material. From a flow and pressure control perspective, such a design is typically operated by setting the injection pumps to a constant injection rate and the back-pressure pump to a constant pressure (constant pressure receive mode). For both injection and back pressure, single-stroke piston pumps are commonly used. Alternatively, dual-piston pumps can be used that provide continuous flow without creating any pressure pulses through zero-displacement valve manifolds. Manufacturers of commonly used pumps include ISCO, Vinci, Quizzix, Cetoni and Vindum. In selecting pumps, attention needs to be paid to the required fluid volume for an entire experiment or re-filling arrangements need to be put in place, and the (pulse-free) minimum flow rate attainable for specific models.

For specific experiments it is also possible to control flow rate through a low-permeable porous disk at the outflow of the core holder [8,69]. In that control design, the injection pumps will be operated by constant pressure. The flow rate is simply controlled by the lowest-permeable element in the system which is the porous disk. The advantage of the design is that it is quite robust against any perturbation by e.g., rotation and bending of flow lines. The disadvantage is that the low-permeable disk will not allow non-wetting phases to pass though. The non-wetting phases will therefore accumulate in front of the low-permeable disk. This may be permissible in some cases, but not in other cases.

Depending on temperature conditions and fluid composition, the wetted parts of the high-pressure pumps may need to be manufactured out of a high nickel alloy such as Hastelloy-C. Stainless steel will not be corrosion resistant to saline brines above room temperature.

5.5. Choice of flow lines and minimizing dead volume

Fluid flow in porous media experimental set-ups, inevitably, accommodates some dead space, mainly, within the tubing, fittings, and the flow cell. For the latter the dead space is predominately at both ends of the sample where the end pieces meet the sample, see Fig. 4a. Considering the small sample volumes used in these experiments a small dead space can become significant. For a sample with diameter of D, length of L, and porosity of ϕ, a gap of ϕL at the core inlet can introduce a dead space equivalent to one pore volume (PV). As such, the impact becomes more significant for tighter samples. For instance, for a typical μCT sample (D=5 mm, L=20 mm, ϕ=30%) the PV is close to 118 μL, equivalent to a gap of 6 mm at core ends. Further, in dynamic μCT-based flow experiments fluid injections are typically performed under constant flow rates of a few μL/min or slower to stay within the capillary dominated flow regime[147] and to allow enough time for dynamic imaging to take place. For such slow flow rates having dead volumes as small as for instance 100 μL results in hundreds of minutes of delay for the displacing fluid to arrive at the inlet face of the sample. This becomes more limiting when the imaging is performed at a synchrotron facility where time is of essence.

The dead space within the flow lines can become significant if those with larger inside diameter are used. As μCT imaging involves rotation of the flow cell, longer injection flow lines are required to allow for the rotation to occur without pulling on the flow cell. As discussed earlier to minimise the dead volume the injection pump can be integrated with the flow cell which provided better control on the injection/imaging procedure (Fig. 4b) [15]. Such flow cells can include one micro-pump for unsteady-state type experiments, or two micro-pumps for fractional flow experiments [148]. The original reason for the design was to avoid the bending of flow lines during the rotation of the sample on the rotation stage (required for the tomography) and any associated impracticalities and potentially associated displacement of fluid inside the flow line (which can be comparable to the flow rate desired in the experiment, depending on experimental conditions and flow lines used). Flow lines connecting the flow cell and external pumps limit the rotation of the cell to 180 or 360 degrees (or a few rotations max) which would require to operate 4D imaging experiments in mode where the cell is rotated back and forth all the time. The imaging is not only delayed but it completely misses the advantages of a continuous rotation mode such as demonstrated in the study by Armstrong et al. (2014) [149] and later perfected by the group from Ghent University in their benchtop system with a gantry [150]. Advances in acquisition trajectories and reconstruction algorithms have also shown to alleviate issues associated with

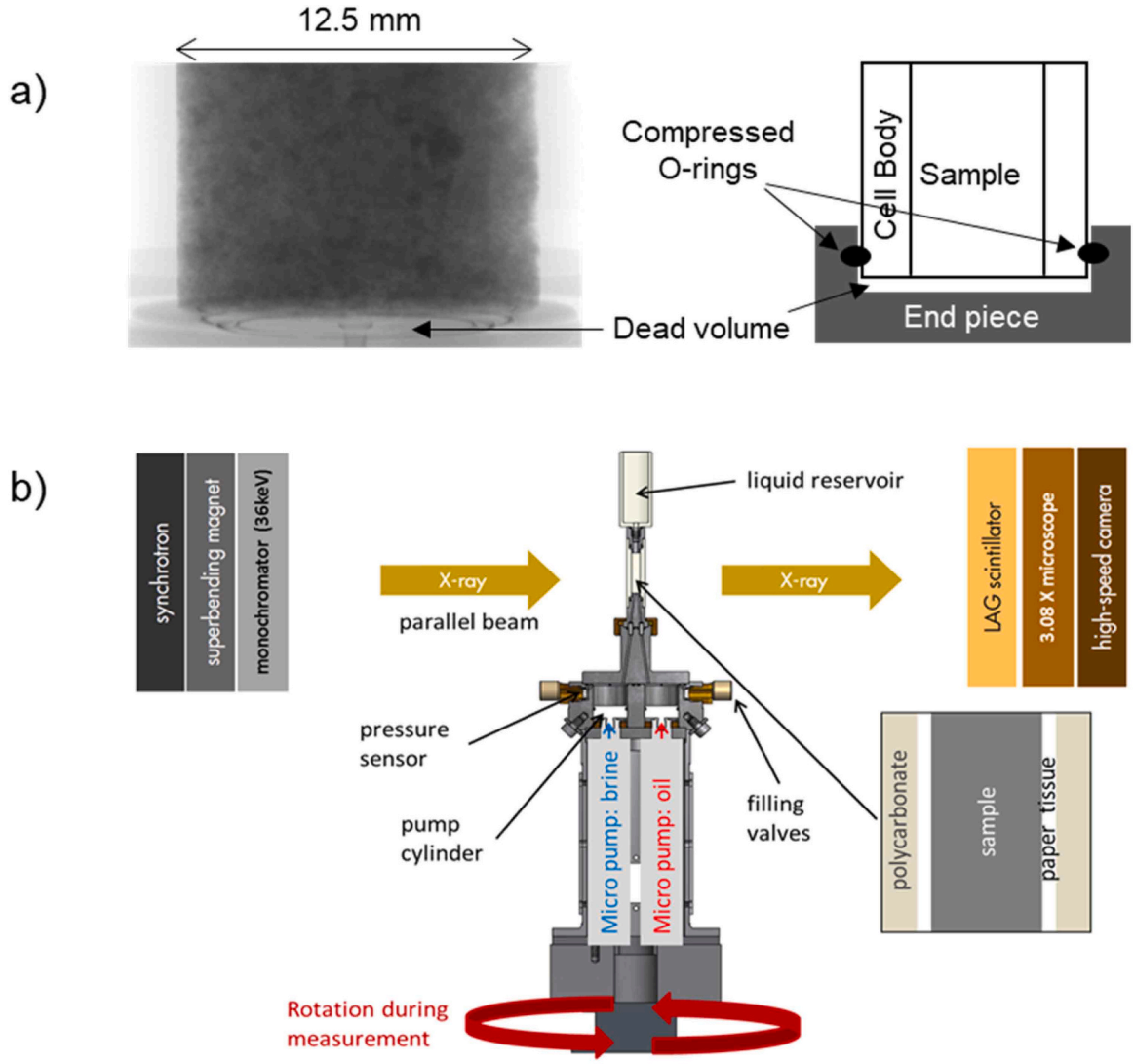

Fig. 4. (a) An example of a typical source of dead space within a flow cell, (b) Flow cell designed by Rucker et al. (2015) [16] that has an integrated injection pump at the injection side of the flow cell to minimize dead volume. It has a built-in micro-pump and does not require any external flow lines during the experiment.

continuous circular imaging, e.g., space-filling trajectories [151].

The ideal scenario is that in 4D experiments, one should continuously acquire projections before specifying reconstruction intervals. In the 2nd step, the time sequence of projections is analysed for displacement events in the porous sample and then reconstruction intervals outside of these displacement events are selected which largely suppresses motion artefacts as displayed in Fig. 5. Beyond suppression of motion artefacts this approach can be combined with modern iterative or maximum expectation reconstruction methods [152] where in a 4D experiment individual reconstructions require significantly fewer projections, which further increases the time resolution.

A continuous rotation of the flow cell is possible either by using an in-situ micro pump or a gantry setup. The latter is possible at benchtop systems such as the one at Ghent University [153] but not at synchrotron beamlines At the time of writing this paper the only commercially available vertical gantry system is the one developed at Ghent University and commercialised as DynaTOM by TESCAN-XRE (there are several other commercial horizontal gantry systems, e.g., by Bruker – model 1276). It is worth noting that acquiring such solutions require significant investment in equipment/development time. Another limitation is continuous streaming of the collected data from the detector. Systems such as the GigaFRoST camera which is an in-house development at the Swiss Light Source allow continuous and sustained data streaming at the rates approaching 8 GB/s, pushing the limits of data acquisition [154]. This is also a storage-heavy approach, with many terabytes of data being generated. In terms of defining the state of the art the means to store, transport and sensibly work through such huge data volumes are critical.

The design/construction of a flow cell with a built-in micro-pump has the advantage of no external flow lines and a pulse-free injection (with gear boxes). The disadvantage, however, is the limited range of injection volume and pressure to less than 0.5 MPa which limits the use of higher back pressures. In absence of sufficient back pressure, in particular, at synchrotron-beamline based experiments, there is a risk of gas bubble formation (see Section 6.5 for more details). It is worth noting that the occurrence or lack of bubble generation is known to be linked with the X-ray irradiation. For instance, to suppress bubble formation back pressures of up to 3 MPa are necessary at the Advanced Photon Source (APS) synchrotron, whereas back pressure of 0.5–1 MPa have proved sufficient at the Brazilian Synchrotron (LNLS) [14]. In contrast, systems such as the HADES triaxial deformation rig build high pressure pumps onto a platform with the cell [155].

For most situations, therefore, designs with external pumps and strategies such as selecting smaller diameter flow lines (typically 1/16th inch) should be considered to keep the dead space minimised. It should be noted that use of such small diameter flow lines may not be suitable for very viscous or non-Newtonian fluids (e.g., colloidal suspensions), where 1/16th inch flow lines may restrict the flow or may require higher pressures. In such cases 1/8th inch flow lines are used but at the cost of increasing the dead volume and injection time by a factor of 40 (the relevant measure is the inner diameter of the tubing. If using 0.01" ID 1/16" tubing versus standard 1/16" ID 1/8" tubing, then the ratio of areas is close to 40 x greater for the 1/8" tubing.). One possible solution is to build small transfer vessels into the base of the flow cell to allow storage of fluids and switching between fluids as per the planned injection sequence. However, this solution is less useful for the case of colloidal suspensions that need to be mixed (or sonicated) constantly during the injection to ensure particles stay suspended [14].

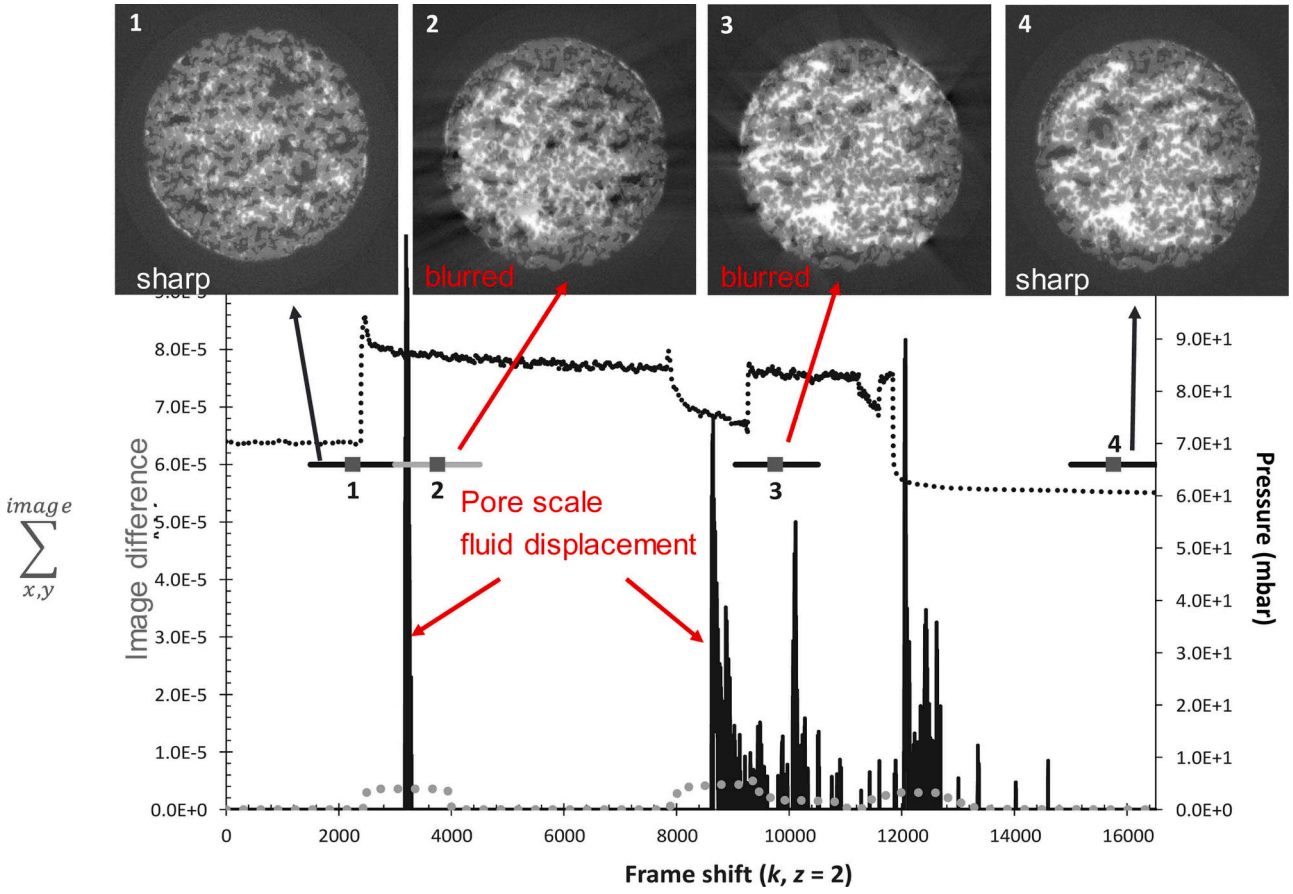

Fig. 5. Displacement event histogram vs. acquisition frame (or time) shown at the bottom. The event histogram shows time periods where fluid-fluid displacements occur inside a porous sample. Intervals without displacement events produce sharp reconstructions while intervals with displacement events suffer from motion artefacts (top row) [149].

5.6. Establishing well-controlled boundary conditions

In a study of fluid flow in porous media it is essential to ensure the flow is well-controlled, e.g., is one dimensional which means the flow happens from the core inlet towards its outlet. In conventional flow cell designs the core is placed in a sleeve (jacket) which is surrounded by a fluid that is used to apply a confining pressure to the core. The confining pressure needs to be kept higher than the pore-pressure to ensure the one dimensionality of the flow. A simpler design for lower pressure ranges is to encapsulate the core in a hard sleeve (typically epoxy resin) which can withstand the pore-pressure. The limitation is, however, that the epoxy resin can penetrate the sample from the pores open to its surrounding. This becomes a more significant issue for smaller samples with very open or vuggy porosity and for thinner epoxies. To overcome this problem the core can be wrapped in a thin film (e.g., aluminium) prior to epoxy casting. However, this can cause problems discussed in the next section.

For the production side, there is typically only a single outlet. However, few designs use a porous plate at the outlet to avoid the non-wetting phase to leave or utilise the low permeability of the porous plate to control the overall pressure drop and flow rate[146]. This outflow boundary condition is also important to consider when interpretating experiments.

6. Potential design limitations

In this section we discuss common limitations faced in multiphase fluid flow in porous media studies with μCT imaging. To have reliable outcomes the following experimental issues and artefacts need to be considered and suppressed.

6.1. Bypassing the porous media (internal leak)

A primary design limitation for these flow cells occurs when the injected fluid finds a preferential flow pathway around the core, this is specifically relevant to those designs with no confining fluid. Figs. 6a and 6b show an example in which a doped oil was to be injected into a carbonate core but has instead by-passed the rock by flowing around the core which poses lower resistance to the flow. This problem is specific to designs that wrap the core using aluminium foil and have no confining pressure. The foil jacket can provide a preferential flow pathway to the injected fluid potentially by-passing the core.

Potential solutions are to wrap the core plug in a sleeve such as heat-shrinkable Teflon sleeve, Viton rubber sleeve or simply using several layers of aluminium foil /Teflon tape is the common practice. It is important to note that finding a suitable sleeve material and method of wrapping is essential in particular when the studied sample is small and the studied fluids include gases and more particularly gasses with high diffusion rates such as hydrogen.

6.2. Set-up rigidity

Weight of the assembly and movements at the ends need to be considered. The flow cell needs to be rigid to avoid sample movements during the imaging. To achieve this, two main considerations are: (i) the weight of the connections hanging at the top end of the flow cell, (ii) the flexibility of the material from which the body is manufactured. Even minor vibrations or movements can result in blurred images. On this basis it is best to avoid using heavy (metal) end pieces along with flexible bodies (e.g. tubes). If required, reinforcement can be put in place to provide additional support for minimising the lateral movements, for instance (i) the cell can be cast in an additional layer of epoxy, externally, or (ii) as shown in Fig. 6c a system of support rods and plates can be used to keep the cell firmly in place[56]. The former approach limits change of sample while the latter solution may cause additional image artefacts generated by the support rods.

6.3. Organic phase preferentially wetting the sleeve

As discussed, the core plugs used in μCT-based studies are typically of a few mm diameter. This means a significant proportion of the pores can be connected to/impacted by the pores that are touching the core boundaries. For the designs that involve encapsulating the core in a plastic-based jacket the fluid distribution can be influenced by (i) preference of the organic phase to flow through the pores that are connected to the oil-wet jacket, and (ii) spontaneous imbibition of the organic phase into the jacket. Fig. 7 shows an example where the oil phase (red) has preferentially occupied the pores that are close to the core surrounding where an oil-wet jacket was present (not shown here). This becomes a more significant issue for smaller samples, i.e., a more substantial boundary effect is in play. One way to overcome this problem is to wrap the sample in another layer (a filter paper, an aluminium sheet, or both) prior to applying the plastic sleeve to avoid direct contact between the oil and the oil-wet jacket.

6.4. Capillary-end effect

Due to the capillary discontinuity at the core outlet the wetting fluid is commonly accumulated within a region close to the core outlet. This is known as the capillary-end effect [156] and is a well-known artefact in core-flooding experiments. It is responsible for artificial fluid occupancies near the core outlet. To overcome this the measurements are commonly performed at higher flow rates (viscous-dominated flow regime), using a long core, or by placing an end piece at the core outlet to "move" the capillary affected zone outside the sample under investigation (in that sense the end piece simply extends the porous media domain). In μCT-based studies it is possible to directly identify this capillary-impacted zone and hence it can be avoided in data analysis. This is only possible if the sample is sufficiently long, hence a priori

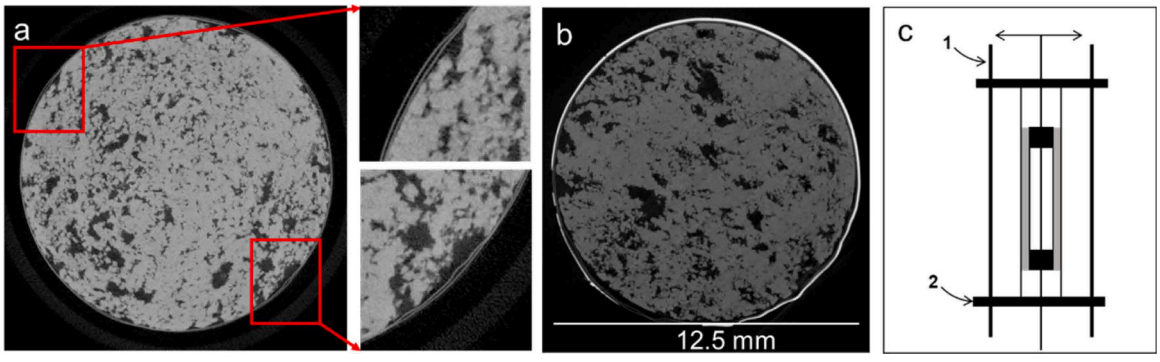

Fig. 6. (a) Core wrapped in multiple layers of aluminium foil, (b) Oil (bright phase, doped) has by-passed the core, (c) core holder movement to the sides at the top end can be minimised through use of(1) support rods, and (2) plates, which eliminate possible movements during imaging.

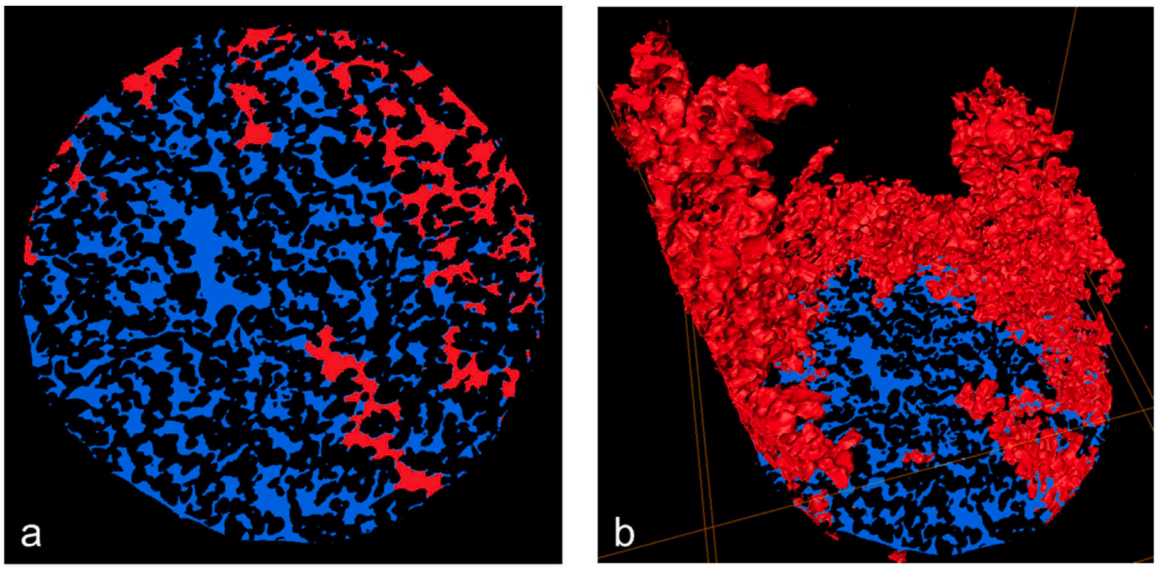

Fig. 7. Preference of an organic fluid (decane) to attach to a (oil-wet) plastic sleeve (not shown here) has caused an artificial distribution of fluids in 3D. Blue: brine, Red: decane, (A) An example 2D slice of the core, (B) 3D rendering of oil. Sample diameter is 3 mm, and it is made of sintered glass.

knowledge of the scale of the affected zone is essential. For homogeneous rocks such as sandstones flow simulation studies performed at core-scale have shown that the capillary end-effect is only pronounced within a 4–5 mm section at the core outlet (L=20 mm)[156]. For more complicated (e.g., dual-porosity) systems this capillary-affected zone can be longer. For instance, for a vuggy carbonate the capillary-end effect was recorded within a 15 mm zone close to core outlet (L=44 mm)[55]. Another option is to explicitly include the capillary end-effect in the analysis and interpretation of the experiment which is well-established at the Darcy scale [157–160]. For a full discussion of the topic, we refer to the special core analysis (SCAL) literature [157–160].

6.5. *Gas bubble formation*

Another challenge that has been encountered during μCT-based imaging studies is generation/entrapment of unwanted air/gas bubbles within the pore-space of the sample. In most cases the presence of an unwanted gas phase cannot be ignored as (i) it introduces additional complexities to the fluid displacement events, (ii) air can be mistaken for any other non-doped fluid, making fluid segmentation challenging, (iii) working with a small sample means that there are limited number of pores available (away from the sample boundaries and outlet) within which the expected dynamics can be studied. Air can occupy some of these pores making the usable volume even smaller.

While interaction of X-rays with the flow cell and the fluids inside leads only to a marginal increase in temperature (fractions of a degree), it can cause formation of gas bubbles because of photochemical effects with contrast agents. This is dependent on X-ray energy, choice of fluids and contrast agents, among other factors. The root cause is not fully understood but photochemical reduction processes might play a role. Most of the studies that reported problems with bubble formation operated at relatively low X-ray energies (below 30 kV) while studies at higher X-ray energies report less risk of bubble formation. The formation of gas bubbles can be suppressed by operating at elevated pressures, e.g., 0.5–1 MPa, which in turn has consequences on the requirement of a back pressure controller and design of the flow cell[161]. The bubble formation is more relevant to synchrotron-based studies, where the X-ray flux is high and therefore fluid interaction with the incident beam can result in phase changes and bubble formation. Irrespective of the X-ray energy selected laboratory-based imaging studies have not reported bubble formation.

7. Comparison of the existing X-ray transparent flow cell designs

Table 3 lists the design specifications of several X-ray transparent flow cells reported in the literature. The information is put together to highlight the cell design considering the application, operating conditions, and the μCT instrument used.

8. Example X-ray transparent flow cells

In this section we discuss the design of four example X-ray transparent flow cells which have been used successfully in practice with the main purpose to serve as basis for future designs. The selected flow cells presented here include designs used for multiphase flow in geological samples as well as electrochemical devices. Also, we have chosen designs that have been successfully used with synchrotron and/or laboratory-based instruments [29,143,166].

8.1. *Shell design - PEEK flow cell for multiphase flow in rocks/columns*

The first cell (shown in Fig. 8) is a PEEK based flow cell which was used in a two-phase flow experiment involving brine and crude oil[82]. This cell is suitable for pressures up to 30 bar and temperatures up to 30 degrees C, and has a back pressure. Clearly visible are the attached flow lines (also made of PEEK, for fluid inflow and outflow), and the sleeve. A special feature of this flow cell is the steel cylinder at its bottom which contains a pressure container to sustain sleeve pressure (pressurised with e.g., N_2) enabling the cell operation with only 2 flow lines attached (inflow and outflow). This is an advantage that makes the experiment more manageable considering the requirement for cell rotation during image acquisition.

The cell had been originally designed to study slow processes such as ageing (which can take several weeks) and shutting in the sample at fixed pressure using built-in valves, and subsequently disconnecting all external flow lines and place the sample in an oven. To compensate for small leaks, a larger pressure vessel was incorporated into the bottom of the cell.

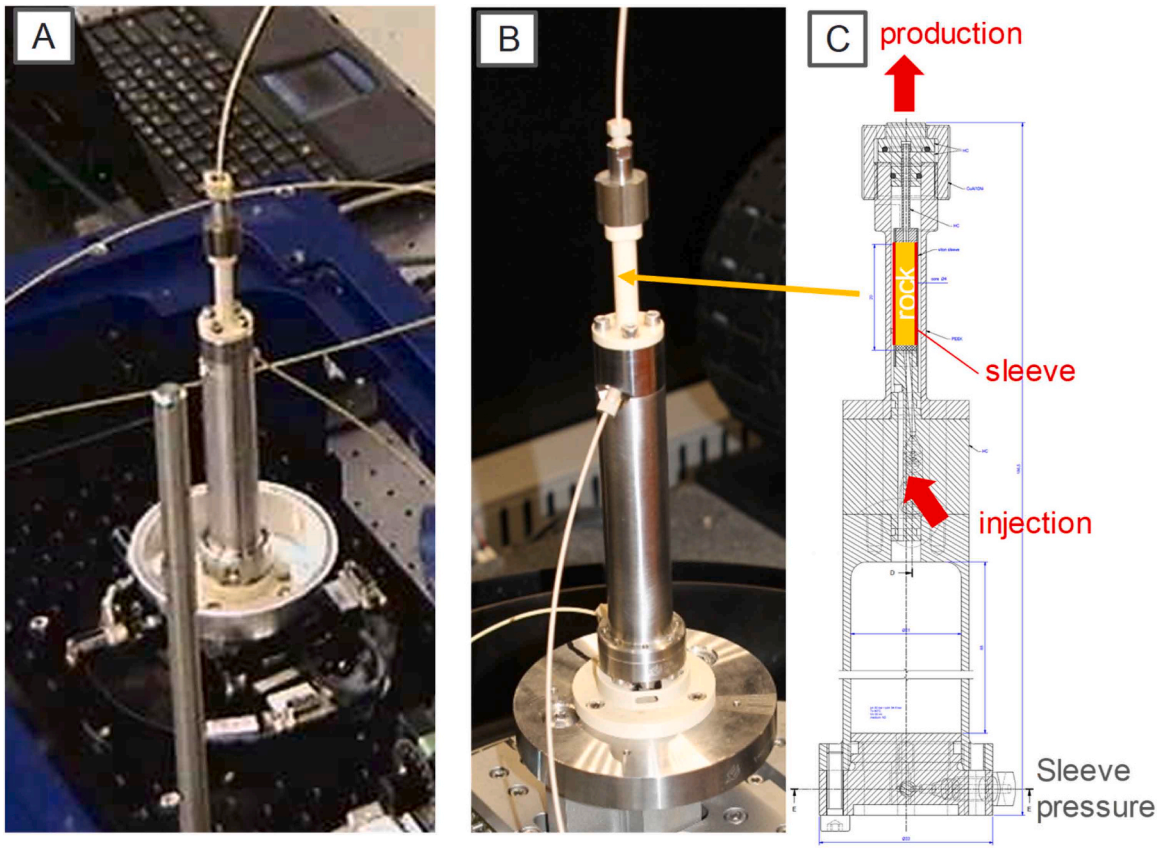

Fig. 8. (A) peek-based flow cell on the rotation state in a synchrotron beamline, (B) during testing in a benchtop micro-CT and (C) construction drawing showing details such as sleeve, injection system and pressure container to maintain sleeve pressure even when sleeve pressure line is not attached.

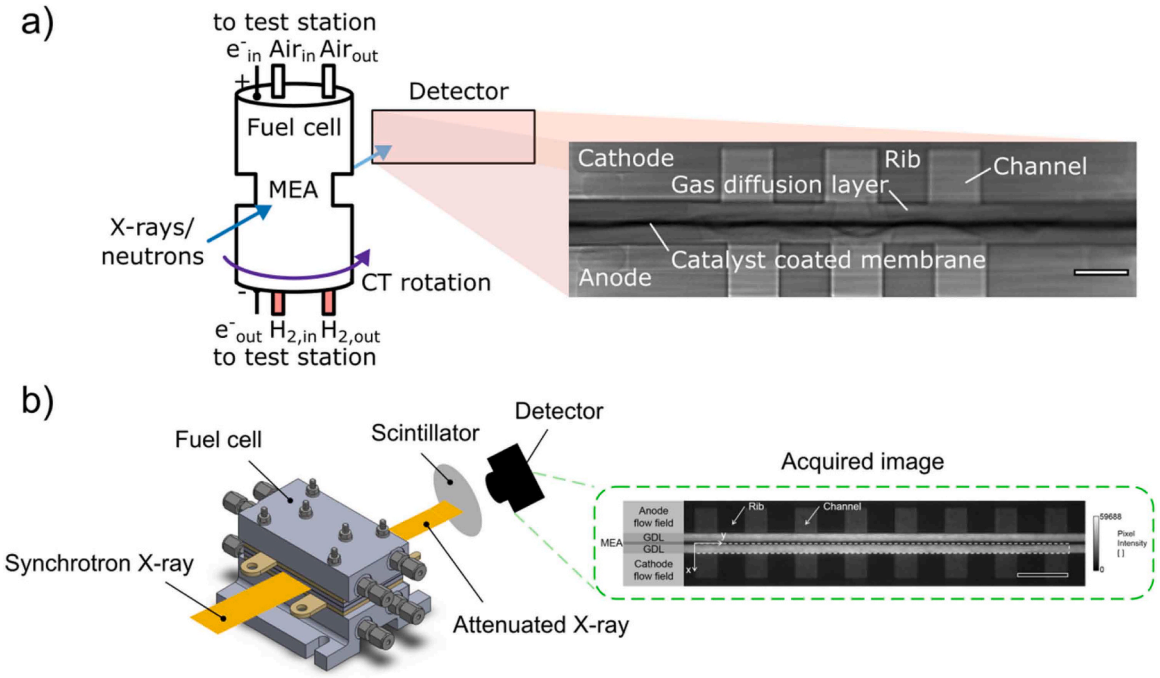

Fig. 9. (A) schematic of the X-ray (a) 3D CT and (b) radiography setup for applications to fuel cells operando. The incident beam becomes attenuated as they penetrate through the membrane electrode assembly of the operating fuel cell. The attenuated beams are then captured by the detector. Scale bar represents 0.5 mm for (a) and 1 mm for (b) [102,106,112].

8.2. University of Toronto design - flow cell for electrochemical devices

The second flow cell we discuss is a flow cell for imaging multiphase flow processes such as gas bubbles in gas diffusion layers. As discussed earlier the challenge is ultimately to allow for the simultaneous transport of gases to the proton exchange membrane and the transport of water to keep the membrane hydrated. This is the rate-limiting factor for the overall device performance. Due to the complexities, it is difficult to model all processes from first principles in a fully coupled way. Therefore, operando imaging is key.

The flow cell in Fig. 9 can sustain pressure up to 3 MPa and temperature up to 60 C. The cell was also used in a study of gas-hydrocarbon mixtures to understand the mechanism by which gas comes out of solution when the pressure declines below the bubble point [174].

8.3. TU Delft design - carbon-fibre epoxy-based flow cell

Flow cells equipped with a sleeve display significant flexibility and can be used for a wide range of samples and types of experiments and have also the advantage that samples are re-usable, i.e., can be taken out e.g., for cleaning by Soxhlet extraction and mounted back in. They have, however, the disadvantage of significant complexity, effort and cost required for manufacturing. In contrast much simpler and lower cost flow cells exist such as the cell design from TU Delft[175]. In this design the cylindrical porous sample is coated stepwise with an epoxy resin applying a thin coating at each step to prevent glue from penetration into the pore space and the reduce the chance of trapping air bubbles in the sleeve. The end pieces manufactured from e.g., plexiglass or polycarbonate with attached flow lines are glued-in as well. The whole assembly is then glued into a carbon fibre epoxy tube as shown in Fig. 10a.

Depending on diameter of the core and the strength of the carbon fibre tube, the pressure rating can go up to 10 MPa. But since no sleeve pressure is applied, the core may deform unevenly. As long as fluids are used which can be cleaned in-situ (e.g., using iso-propanol) the flow cell is re-usable but does not present a generally re-usable case as a design with sleeve.

8.4. University of Edinburgh design - carbon fibre pressure cell

Here we present the technical drawings for a simple flow cell with high transparency, (see the supporting information file 2). This is a carbon fibre composite pressure cell (see Fig. 10b) which uses commonly obtainable materials and can be readily manufactured in any machine shop with a suitable lathe and milling machine. The cell was built at the School of Geosciences, University of Edinburgh and has been used to image multiphase fluid flow experiments on a laboratory μCT instrument with confining pressure of 10 MPa and pore pressure of 5 MPa. The cell was operated at these pressures for 6 weeks continuously, and so offers a simple, high transparency solution to access fluid flow experiments at elevated pressure for modest cost. A description of the cell manufacture and assembly is included and can be found in the Supplementary Information file, section S2.

9. Practical approach to designing an experimental setup and safety aspects

Next to all the engineering challenges, there also several non-technical risks that need to be addressed by the design. The starting point in building a flow cell is to understand the local testing and insurance requirements and to ensure that these considerations are properly addressed in the design. This is to ensure that the experiment will be compliant with the institution's legal health and safety requirements. The specifics of these requirements depend upon local legal and insurance requirements. We note that these requirements differ from country to country and institution to institution (in the case of insurance) so we encourage the readers to explore the relevant requirement that applies to their institution and country.

In this section we share guidance on designing a flow cell by building on an existing design or through putting in place a new design.

9.1. Using an existing design as starting point

The easiest approach is to use an existing design (see the studies listed in Table 3, and the example designs discussed in Section 8) as starting point and adapt it for the intended purpose. If in the intended

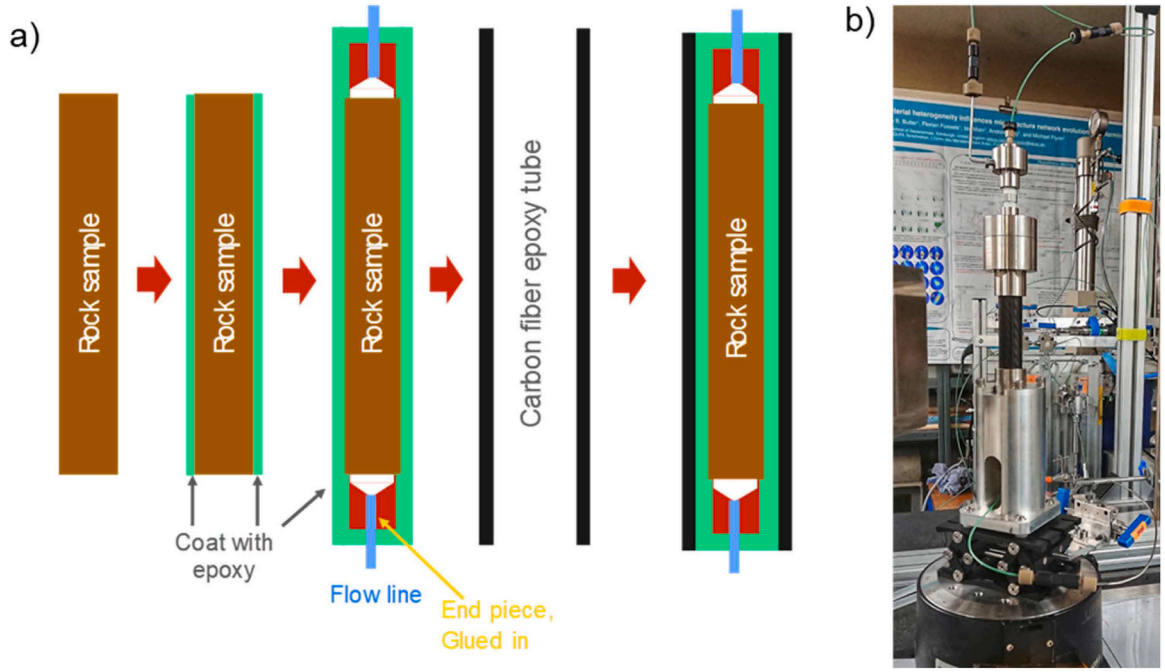

Fig. 10. (a) The TU Delft cell that is composed of carbon-fibre epoxy tube with rock sample and flow lines glued-in using epoxy resin [175], (b) University of Edinburgh flow cell, which is a composite of steel structural components, and a carbon fibre pressure vessel.

application the pressure/temperature combination exceeds the one in the listed design, a new mechanical stability calculation needs to be made. Also, if different fluids e.g., organic solvents[176] or supercritical CO_2 [8] are used, the material compatibility with pressure vessel and seals needs to be checked.

9.1.1. New designs

For an entirely new design, logical starting points are (a) requirements on the pressure vessel in terms of length/width, pressure, temperature, (b) limitations that the intended laboratory μCT instruments or synchrotron beamline imposes in terms of dimensions of the flow cell and total weight but also X-ray energy and total flux. In particular synchrotron beamlines can vary significantly in terms of characteristics such as size of the beam, but also beam energy see Table 2. The beam energy may impose limitations for the choice of materials for the flow cell.

Benchtop μCT instruments often impose significant limitations on the minimum distance of the area of interest i.e., the inside of the flow cell, from the X-ray source, which may limit the maximum wall thickness of the flow cell. Also, the end flanges may need to be positioned below and above the X-ray tube to minimize the distance to window of the X-ray tube. The exact details can also vary significantly depending on the type of μCT instrument used. Systems with a classical cone beam geometry and geometric magnification only require typically shorter distances to the outlet window of the X-ray tube, while systems which also use optical magnification allow more flexibility. Gantry-based systems can handle flow lines more easily than traditional systems where the flow cell needs to rotate and requires a system for handling the flow lines, i.e., preventing them becoming entangled inside the instrument. Some μCT vendors offer special kits for flow line handling.

The next important question to answer is whether a single-use flow cell will be suitable, or whether a re-usable design with a sleeve construction is needed. A conceptual overview of the design flowchart is displayed in Fig. 11.

If an already established design can be adapted, only minor modifications might be required. However, mechanical strength calculations may need to be re-done. For a new design, logical starting points are either the pressure and temperature requirements, or the limitations of the beamline in terms of beam geometry, energy, and flux. For a new design, one may follow either the route of core holder design based on temperature range or based on pressure range:

9.1.2. Design based on temperature range

Most of the flow cells used in practice (Table 3) operate at low/ambient temperatures. For low temperature conditions flow cells can be made from non-metallic materials in particular polymers (such as Plexiglass, Perspex, polypropylene, and epoxy resin),. These materials also have the advantage of being low cost.

For cases where moderate temperature conditions are needed materials such as PEEK, poly-methyl-methacrylate (PMMA), and polycarbonate can be used. These offer higher thermal stability and lower X-ray absorption compared to metals. However, PMMA has typically an upper bound to the operating temperature around 70–85 °C, while polycarbonate, depending on the exact type, typically goes beyond that.

For high temperature environments such as where thermal degradation/decomposition of material/minerals is studied flow cell needs to be made of metals or metal alloys [29,143,166]. These have the disadvantage of absorbing a significant proportion of the flux of the incident X-ray beam and, therefore, resulting in lower signal to noise ratios for the produced images. The main metal used is aluminium (and its alloys). Some studies have used Titanium and even stainless steel (where the mechanical strength is needed).

Other materials used to make the flow cell body for the studies listed in Table 3 include carbon fibre composite and glass (columns commonly used in standard chromatography). The carbon fibre composite offers good X-ray transparency. Glass (depending on the type used) can offer relatively moderate X-ray transparency.

9.1.3. Design based on pressure range

The maximum allowable operating pressure for a flow cell depends

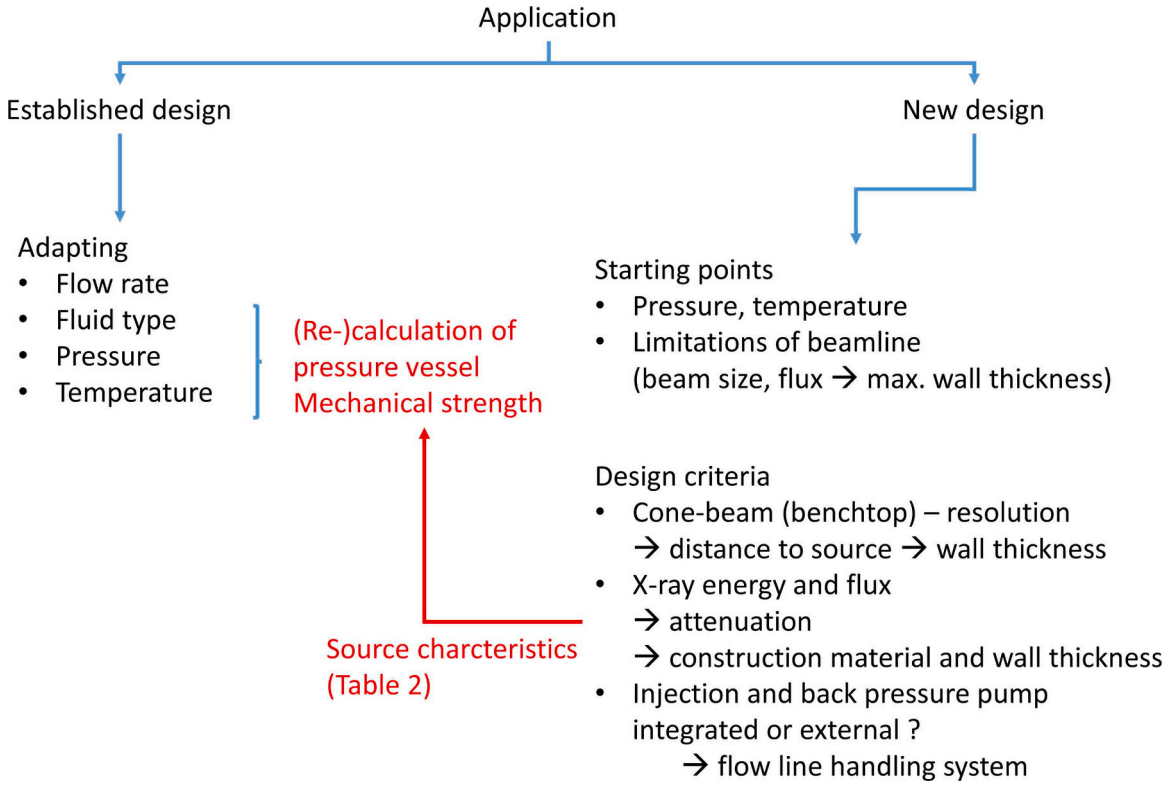

Fig. 11. Steps taken in designing μCT compatible flow cells for a specific application.

both on the material used and the cell design (including the wall thickness, the assembly mechanism used, and the seal). While plastic materials have mostly been used to study low pressure conditions there are a range of high tensile strength plastics and polymers such as PEEK and polyamidimid that can be used in moderate pressure designs.

The high-pressure flow cells are made of metals (such as aluminium and titanium) and composite material such as (carbon fibre). This allows studying dynamic processes at conditions closer to reality for example for studies investigating the deep subsurface environments (e.g., CO_2 and hydrogen storage).

9.2. *Pressure vessels and safety aspects*

For cells designed to work at elevated pressures, the flow cell is considered a pressure vessel and respective mechanical strength calculations need to be conducted but a qualified design engineer [177,178]. In many cases that involves a design in a CAD software and finite element calculations on the mechanical strength. There are also commercially available flow cells which may satisfy most of the regulatory requirements, e.g., flow cells from RS Systems (RS Systems AS, FOSNAVÅG, Norway). Finally, a pressure test is required before the system can be put into use.

9.3. *Incorporation of sensors [146]*

An additional aspect can be the incorporation of sensors into the flow cell, such as pressure sensors [15], differential pressure sensors, temperature sensors, etc. [179–181]. Some pressure sensors are resistant to aqueous fluids but not to organic fluids including oils, n-decane and organic solvents. The fluid compatibility needs to be established and tested upfront. If needed the pressure sensor can be protected from direct contact with an oil phase by placing a small volume of water in-between. However, that approach might not be successful if the organic phase e.g., a solvent is soluble in water.

Individual pressure sensors might have offsets which need to be calibrated first. Differential pressure transducers are more reliable in this regard but require flow lines from inlet and outlet to the sensor, which might impose extra limitations on the flow line handling for rotating samples. Large height differences between inlet and outlet may need to be corrected for a gravity head.

10. Summary and conclusions

This contribution presents a review of laboratory systems used over the past decades to study fluid flow within porous media non-destructively and using X-ray μCT technique. We discuss the main applications that have benefitted from μCT-based dynamic experiments and highlight open research areas that can be advanced through μCT imaging studies. With the current technology of X-ray μCT imaging, 3D images of opaque samples can be produced down to sub-micrometre scale resolution. In terms of image resolution both synchrotron facilities and laboratory-based μCT instruments can achieve sub-micron resolutions if a sufficiently small samples (typically of the order of few mms) are used. Typical imaging times for laboratory-based instrument have reduced significantly over the past decade. This means that with some laboratory-based systems 3D images can be captured in seconds, approaching what is achievable in synchrotron facilities. However, the conventional laboratory-based instruments are still much slower, typically taking minutes to hours to produce a 3D image.

As an important component of μCT studies we discussed the design and limitations of X-ray transparent flow cells suitable for these studies. We present a comprehensive discussion of the design requirements, limitations, and challenges. This review also presents some practical ways to overcome the highlighted challenges. Finally, we propose a workflow and highlight the key decisions and considerations that need to be considered to design a μCT-compatible flow cell in compliance with local legal and insurance requirements.

Declaration of Competing Interest

The authors declare the following financial interests/personal relationships which may be considered as potential competing interests: Ian B. Butler reports financial support was provided by Petrobras and Shell that sponsored the International Centre for Carbonate Reservoirs (ICCR).

Acknowledgment

The authors would like to thank Petrobras and Shell for their sponsorship of the International Centre for Carbonate Reservoirs (ICCR), and for permission to publish the carbon fibre cell design presented in this work.

Appendix A. Supporting information

Supplementary data associated with this article can be found in the online version at doi:10.1016/j.tmater.2023.100017.

References

[1] D. Wildenschild, A.P. Sheppard, X-ray imaging and analysis techniques for quantifying pore-scale structure and processes in subsurface porous medium systems, Adv. Water Resour. vol. 51 (. 2013) 217–246, https://doi.org/10.1016/j.advwatres.2012.07.018.

[2] F. Fusseis, X. Xiao, C. Schrank, F. De Carlo, A brief guide to synchrotron radiation-based microtomography in (structural) geology and rock mechanics, J. Struct. Geol. vol. 65 (2014) 1–16, https://doi.org/10.1016/j.jsg.2014.02.005.

[3] V. Cnudde, M.N. Boone, High-resolution X-ray computed tomography in geosciences: a review of the current technology and applications, Earth-Sci. Rev. vol. 123 (2013) 1–17, https://doi.org/10.1016/j.earscirev.2013.04.003.

[4] L. Salvo, et al., X-ray micro-tomography an attractive characterisation technique in materials science, Nucl. Instrum. Methods Phys. Res., Sect. B: Beam Interact. Mater. At. (2003) 273–286, https://doi.org/10.1016/S0168-583X(02)01689-0.

[5] S. Schlüter, A. Sheppard, K. Brown, D. Wildenschild, Image processing of multiphase images obtained via X-ray microtomography: a review, Water Resour. Res. vol. 50 (4) (2014) 3615–3639, https://doi.org/10.1002/2014WR015256.

[6] A. Sheppard, et al., Techniques in helical scanning, dynamic imaging and image segmentation for improved quantitative analysis with X-ray micro-CT, Nucl. Instrum. Methods Phys. Res B vol. 324 (2014) 49–56, https://doi.org/10.1016/j.nimb.2013.08.072.

[7] R.T. Armstrong, M.L. Porter, D. Wildenschild, Linking pore-scale interfacial curvature to column-scale capillary pressure, Adv. Water Resour. vol. 46 (. 2012) 55–62, https://doi.org/10.1016/J.ADVWATRES.2012.05.009.

[8] M. Andrew, B. Bijeljic, M.J. Blunt, Pore-scale imaging of trapped supercritical carbon dioxide in sandstones and carbonates, Int. J. Greenh. Gas. Control vol. 22 (2014) 1–14, https://doi.org/10.1016/j.ijggc.2013.12.018.

[9] K. Singh, B. Bijeljic, M.J. Blunt, Imaging of oil layers, curvature and contact angle in a mixed-wet and a water-wet carbonate rock, Water Resour. Res vol. 52 (3) (2016) 1716–1728, https://doi.org/10.1002/2015WR018072.

[10] S. Iglauer, M.A. Fern??, P. Shearing, M.J. Blunt, Comparison of residual oil cluster size distribution, morphology and saturation in oil-wet and water-wet sandstone, J. Colloid Interface Sci. vol. 375 (1) (2012) 187–192, https://doi.org/10.1016/j.jcis.2012.02.025.

[11] B. Bartels et al., Micro-CT study of the Impact of Low Salinity Waterflooding on the pore-scale fluid distribution during flow, *nternational Symposium of the Society of Core Analysts held in Snowmass, Colorado, USA*, 2016.

[12] J. Desarnaud, H. Derluyn, L. Molari, S. De Miranda, V. Cnudde, N. Shahidzadeh, Drying of salt contaminated porous media: effect of primary and secondary nucleation, J. Appl. Phys. (2015), https://doi.org/10.1063/1.4930292.

[13] T. Pak, I.B. Butler, S. Geiger, M.I.J. van Dijke, K.S. Sorbie, Droplet fragmentation: 3D imaging of a previously unidentified pore-scale process during multiphase flow in porous media, Proc. Natl. Acad. Sci. vol. 112 (7) (2015) 1947–1952 ([Online]. Available), ⟨http://www.pnas.org/content/112/7/1947.abstract⟩.

[14] T. Pak, L.F. de L. Luz, T. Tosco, G.S.R. Costa, P.R.R. Rosa, N.L. Archilha, Pore-scale investigation of the use of reactive nanoparticles for in situ remediation of contaminated groundwater source, Proc. Natl. Acad. Sci. vol. 117 (24) (. 2020) 201918683, https://doi.org/10.1073/pnas.1918683117.

[15] S. Berg, et al., Real-time 3D imaging of Haines jumps in porous media flow, pp. 3755–9, Proc. Natl. Acad. Sci. USA vol. 110 (10) (. 2013), https://doi.org/10.1073/pnas.1221373110.

[16] M. Rücker, et al., From connected pathway flow to ganglion dynamics, Geophys Res Lett. vol. 42 (10) (2015) 3888–3894, https://doi.org/10.1002/2015GL064007.

[17] S. Hasan, et al., Direct characterization of solute transport in unsaturated porous media using fast X-ray synchrotron microtomography, Proc. Natl. Acad. Sci. USA (2020), https://doi.org/10.1073/pnas.2011716117.

[18] E.M. Thaysen, et al., Pore-scale imaging of hydrogen displacement and trapping in porous media (Nov), Int J. Hydrog. Energy (2022), https://doi.org/10.1016/J.IJHYDENE.2022.10.153.

[19] M.L. Turner, et al., Three-dimensional imaging of multiphase flow in porous media, *Phys. A: Stat. Mech. its Appl.* (2004) 166–172, https://doi.org/10.1016/j.physa.2004.03.059.

[20] S. Iglauer, S. Favretto, G. Spinelli, G. Schena, M.J. Blunt, X-ray tomography measurements of power-law cluster size distributions for the nonwetting phase in sandstones, Phys. Rev. E Stat. Nonlin Soft Matter Phys. vol. 82 (5) (2010), https://doi.org/10.1103/PhysRevE.82.056315.

[21] Y. Zhang, O. Nishizawa, T. Kiyama, S. Chiyonobu, Z. Xue, Flow behaviour of supercritical CO_2 and brine in Berea sandstone during drainage and imbibition revealed by medical X-ray CT images, Geophys J. Int vol. 197 (3) (. 2014) 1789–1807, https://doi.org/10.1093/gji/ggu089.

[22] T. Pak, N.L. Archilha, I.F. Mantovani, A.C. Moreira, I.B. Butler, An X-ray computed micro-tomography dataset for oil removal from carbonate porous media, Sci. Data vol. 6 (. 2019), 190004, https://doi.org/10.1038/sdata.2019.4.

[23] N.L. Archilha, et al., Permeability and acoustic velocity controlling factors determined from x-ray tomography images of carbonate rocks, Am. Assoc. Pet. Geol. Bull. vol. 100 (8) (2016) 1289–1309, https://doi.org/10.1306/02251615044.

[24] H. Hosseinzade Khanamiri, O. Torsæter, J.Å. Stensen, Effect of calcium in pore scale oil trapping by low-salinity water and surfactant enhanced oil recovery at strongly water-wet conditions: in situ imaging by x-ray microtomography, Energy Fuels (2016), https://doi.org/10.1021/acs.energyfuels.6b01236.

[25] M. Shabaninejad, J. Middlelton, A. Fogden, Systematic pore-scale study of low salinity recovery from Berea sandstone analyzed by micro-CT, J. Pet. Sci. Eng. vol. 163 (. 2018) 283–294, https://doi.org/10.1016/J.PETROL.2017.12.072.

[26] N.K. Jha, et al., Pore scale investigation of low salinity surfactant nanofluid injection into oil saturated sandstone via X-ray micro-tomography, J. Colloid Interface Sci. (2020), https://doi.org/10.1016/j.jcis.2019.12.043.

[27] Y. Chen, et al., Geochemical controls on wettability alteration at pore-scale during low salinity water flooding in sandstone using X-ray micro computed tomography, Fuel (2020), https://doi.org/10.1016/j.fuel.2020.117675.

[28] D. Wang, et al., Study of hydrate occupancy, morphology and microstructure evolution with hydrate dissociation in sediment matrices using X-ray micro-CT, Mar. Pet. Geol. (2020), https://doi.org/10.1016/j.marpetgeo.2019.104138.

[29] M. Chaouachi, et al., Microstructural evolution of gas hydrates in sedimentary matrices observed with synchrotron X-ray computed tomographic microscopy, Geochem. Geophys. Geosyst. vol. 16 (6) (2015) 1711–1722, https://doi.org/10.1002/2015GC005811.

[30] S.A. Klapp, et al., Microstructure characteristics during hydrate formation and dissociation revealed by X-ray tomographic microscopy, Geo-Mar. Lett. (2012), https://doi.org/10.1007/s00367-012-0276-0.

[31] V.V. Nikitin, et al., Dynamic in-situ imaging of methane hydrate formation and self-preservation in porous media, Mar. Pet. Geol. (2020), https://doi.org/10.1016/j.marpetgeo.2020.104234.

[32] R.M. Lieb-Lappen, E.J. Golden, R.W. Obbard, Metrics for interpreting the microstructure of sea ice using X-ray micro-computed tomography, Cold Reg. Sci. Technol. (2017), https://doi.org/10.1016/j.coldregions.2017.03.001.

[33] H. Derluyn, J. Dewanckele, M.N. Boone, V. Cnudde, D. Derome, J. Carmeliet, Crystallization of hydrated and anhydrous salts in porous limestone resolved by synchrotron X-ray microtomography, *Nucl. Instrum. Methods Phys. Res B* (2014), https://doi.org/10.1016/j.nimb.2013.08.065.

[34] H. Derluyn, et al., Characterizing saline uptake and salt distributions in porous limestone with neutron radiography and X-ray micro-tomography, J. Build. Phys. (2013), https://doi.org/10.1177/1744259112473947.

[35] M. Norouzi Rad, N. Shokri, M. Sahimi, Pore-scale dynamics of salt precipitation in drying porous media, Phys. Rev. E vol. 88 (3) (. 2013), 032404, https://doi.org/10.1103/PhysRevE.88.032404.

[36] M.N. Rad, N. Shokri, A. Keshmiri, P.J. Withers, Effects of grain and pore size on salt precipitation during evaporation from porous media, Transp. Porous Media (2015), https://doi.org/10.1007/s11242-015-0515-8.

[37] A. Mularczyk, et al., Droplet and percolation network interactions in a fuel cell gas diffusion layer, J. Electrochem Soc. (2020), https://doi.org/10.1149/1945-7111/ab8c85.

[38] J. Eller, T. Rosén, F. Marone, M. Stampanoni, A. Wokaun, F.N. Büchi, Progress in in situ X-ray tomographic microscopy of liquid water in gas diffusion layers of PEFC, J. Electrochem Soc. (2011), https://doi.org/10.1149/1.3596556.

[39] T. Arlt, M. Klages, M. Messerschmidt, J. Scholta, I. Manke, Influence of artificially aged gas diffusion layers on the water management of polymer electrolyte membrane fuel cells analyzed with in-operando synchrotron imaging, Energy (2017), https://doi.org/10.1016/j.energy.2016.10.061.

[40] F. García-Moreno, et al., Using X-ray tomoscopy to explore the dynamics of foaming metal, Nat. Commun. (2019), https://doi.org/10.1038/s41467-019-11521-1.

[41] D. Hughes, E.H. Amalu, T. Pak, R. Kennedy, Effect of relative density on compressive load response of crumpled aluminium foil mesh, Materials (2019), https://doi.org/10.3390/ma12234018.

[42] R. Mousavi, T. Miri, P.W. Cox, P.J. Fryer, Imaging food freezing using X-ray microtomography, Int J. Food Sci. Technol. (2007), https://doi.org/10.1111/j.1365-2621.2007.01514.x.

[43] K.S. Lim, M. Barigou, X-ray micro-computed tomography of cellular food products, Food Res. Int. (2004), https://doi.org/10.1016/j.foodres.2004.06.010.

[44] J.H. Hubbell, Photon cross sections, attenuation coefficients, and energy absorption coefficients from 10 keV to 100 GeV, *National Standard Reference Data System.*, 1969.

[45] K. Brown, S. Schlüter, A. Sheppard, D. Wildenschild, On the challenges of measuring interfacial characteristics of three-phase fluid flow with x-ray microtomography, J. Microsc. vol. 253 (3) (2014), https://doi.org/10.1111/jmi.12106.

[46] M. Ruf, H. Steeb, An open, modular, and flexible micro X-ray computed tomography system for research, Rev. Sci. Instrum. (2020), https://doi.org/10.1063/5.0019541.

[47] T. Bultreys, et al., Real-time visualization of Haines jumps in sandstone with laboratory-based microcomputed tomography, Water Resour. Res vol. 51 (10) (2015) 8668–8676, https://doi.org/10.1002/2015WR017502.

[48] K. Singh, et al., The role of local instabilities in fluid invasion into permeable media, Sci. Rep. vol. 7 (1) (2017), https://doi.org/10.1038/s41598-017-00191-y.

[49] S. Youssef, et al., 4D imaging of fluid flow dynamics in natural porous media with ultra-fast X-ray microtomography, Int. Symp. . Core Anal. (SCA2013–012) (2013) 1–12.

[50] K. Singh, et al., Dynamics of snap-off and pore-filling events during two-phase fluid flow in permeable media, Sci. Rep. vol. 7 (1) (2017), https://doi.org/10.1038/s41598-017-05204-4.

[51] M. Rücker, et al., From connected pathway flow to ganglion dynamics, Geophys Res Lett. vol. 42 (10) (2015) 3888–3894, https://doi.org/10.1002/2015GL064007.

[52] R.T. Armstrong, J.E. McClure, M.A. Berrill, M. Rücker, S. Schlüter, S. Berg, Beyond Darcy's law: the role of phase topology and ganglion dynamics for two-fluid flow, Phys. Rev. E vol. 94 (4) (2016), https://doi.org/10.1103/PhysRevE.94.043113.

[53] A.L. Herring, L. Andersson, D.L. Newell, J.W. Carey, D. Wildenschild, Pore-scale observations of supercritical CO2drainage in Bentheimer sandstone by synchrotron x-ray imaging, Int. J. Greenh. Gas. Control vol. 25 (2014) 93–101, https://doi.org/10.1016/j.ijggc.2014.04.003.

[54] A.H. Alizadeh, M. Khishvand, M.A. Ioannidis, M. Piri, Multi-scale experimental study of carbonated water injection: an effective process for mobilization and recovery of trapped oil, Fuel vol. 132 (2014) 219–235, https://doi.org/10.1016/j.fuel.2014.04.080.

[55] T. Pak, Saturation tracking and identification of residual oil saturation, University of Edinburgh, 2015. Accessed: May 04, 2017. [Online]. Available: ⟨https://ethos.bl.uk/OrderDetails.do?uin=uk.bl.ethos.700070⟩.

[56] T. Pak et al., Pore-Scale Visualisation of Two-Phase Fluid Displacement Processes in a Carbonate Rock using X-ray micro-TomographyTechnique, in *SPE Reservoir Characterization and Simulation Conference and Exhibition* doi: 10.2118/165997-MS, Sep. 2013.

[57] M. Andrew, B. Bijeljic, M.J. Blunt, Pore-scale contact angle measurements at reservoir conditions using X-ray microtomography, Adv. Water Resour. vol. 68 (2014) 24–31, https://doi.org/10.1016/j.advwatres.2014.02.014.

[58] K.A. Klise, D. Moriarty, H. Yoon, Z. Karpyn, Automated contact angle estimation for three-dimensional X-ray microtomography data, Adv. Water Resour. vol. 95 (2016) 152–160, https://doi.org/10.1016/j.advwatres.2015.11.006.

[59] A. Scanziani, K. Singh, M.J. Blunt, A. Guadagnini, Automatic method for estimation of in situ effective contact angle from X-ray micro tomography images of two-phase flow in porous media, J. Colloid Interface Sci. vol. 496 (2017), https://doi.org/10.1016/j.jcis.2017.02.005.

[60] G. Garfi, C.M. John, Q. Lin, S. Berg, S. Krevor, Fluid surface coverage showing the controls of rock mineralogy on the wetting state, Geophys Res Lett. (2020), https://doi.org/10.1029/2019GL086380.

[61] C. Sun, J.E. McClure, P. Mostaghimi, A.L. Herring, S. Berg, R.T. Armstrong, Probing effective wetting in subsurface systems, Geophys Res Lett. (2020), https://doi.org/10.1029/2019GL086151.

[62] J.E. McClure, et al., Geometric state function for two-fluid flow in porous media, Phys. Rev. Fluids (2018), https://doi.org/10.1103/PhysRevFluids.3.084306.

[63] M. Lebedev, Y. Zhang, V. Mikhaltsevitch, S. Inglauer, T. Rahman, Residual trapping of supercritical CO_2: direct pore-scale observation using a low cost pressure cell for micro computer tomography, Energy Procedia vol. 114 (. 2017) 4967–4974, https://doi.org/10.1016/J.EGYPRO.2017.03.1639.

[64] M. Akbarabadi, M. Piri, Relative permeability hysteresis and capillary trapping characteristics of supercritical CO_2/brine systems: an experimental study at reservoir conditions, Adv. Water Resour. vol. 52 (. 2013) 190–206, https://doi.org/10.1016/J.ADVWATRES.2012.06.014.

[65] L. Zuo, S. Krevor, R.W. Falta, S.M. Benson, An experimental study of CO_2 exsolution and relative permeability measurements during CO_2 saturated water depressurization, Transp. Porous Media vol. 91 (2) (. 2012) 459–478, https://doi.org/10.1007/s11242-011-9854-2.

[66] J.-C. Perrin, S. Benson, An experimental study on the influence of sub-core scale heterogeneities on CO_2 distribution in reservoir rocks, Transp. Porous Media vol. 82 (1) (. 2010) 93–109, https://doi.org/10.1007/s11242-009-9426-x.

[67] A.L. Herring, L. Andersson, S. Schlüter, A. Sheppard, D. Wildenschild, Efficiently engineering pore-scale processes: the role of force dominance and topology during nonwetting phase trapping in porous media, Adv. Water Resour. vol. 79 (2015) 91–102, https://doi.org/10.1016/j.advwatres.2015.02.005.

[68] A.L. Herring, A. Sheppard, L. Andersson, D. Wildenschild, Impact of wettability alteration on 3D nonwetting phase trapping and transport, Int. J. Greenh. Gas. Control vol. 46 (. 2016) 175–186, https://doi.org/10.1016/j.ijggc.2015.12.026.

[69] S. Iglauer, A. Paluszny, C.H. Pentland, M.J. Blunt, Residual CO $_2$ imaged with X-ray micro-tomography (p. n/a-n/a), Geophys Res Lett. vol. 38 (21) (. 2011), https://doi.org/10.1029/2011GL049680.

[70] B.L. Alemu, E. Aker, M. Soldal, Ø. Johnsen, P. Aagaard, Effect of sub-core scale heterogeneities on acoustic and electrical properties of a reservoir rock: a CO $_2$ flooding experiment of brine saturated sandstone in a computed tomography scanner, Geophys Prospect vol. 61 (1) (. 2013) 235–250, https://doi.org/10.1111/j.1365-2478.2012.01061.x.

[71] S. Iglauer, T. Rahman, M. Sarmadivaleh, A. Al-Hinai, M.A. Fernø, M. Lebedev, Influence of wettability on residual gas trapping and enhanced oil recovery in three-phase flow: a pore-scale analysis by use of microcomputed tomography, SPE J. vol. 21 (06) (. 2016) 1916–1929, https://doi.org/10.2118/179727-PA.

[72] D.-X. Du, A.N. Beni, R. Farajzadeh, P.L.J. Zitha, Effect of water solubility on carbon dioxide foam flow in porous media: an x-ray computed tomography study, Ind. Eng. Chem. Res vol. 47 (16) (. 2008) 6298–6306, https://doi.org/10.1021/ie701688j.

[73] S. Higgs, et al., In-situ hydrogen wettability characterisation for underground hydrogen storage, Int J. Hydrog. Energy vol. 47 (26) (. 2022) 13062–13075, https://doi.org/10.1016/J.IJHYDENE.2022.02.022.

[74] N.K. Jha, A. Al-Yaseri, M. Ghasemi, D. Al-Bayati, M. Lebedev, M. Sarmadivaleh, Pore scale investigation of hydrogen injection in sandstone via X-ray micro-tomography, Int J. Hydrog. Energy vol. 46 (70) (. 2021) 34822–34829, https://doi.org/10.1016/J.IJHYDENE.2021.08.042.

[75] M. Khishvand, A.H. Alizadeh, M. Piri, In-situ characterization of wettability and pore-scale displacements during two- and three-phase flow in natural porous media, Adv. Water Resour. vol. 97 (2016) 279–298, https://doi.org/10.1016/j.advwatres.2016.10.009.

[76] A. Scanziani, et al., In situ characterization of three-phase flow in mixed-wet porous media using synchrotron imaging, Water Resour. Res (2020), https://doi.org/10.1029/2020WR027873.

[77] A. Alhosani, et al., Three-phase flow displacement dynamics and Haines jumps in a hydrophobic porous medium, Proc. R. Soc. A: Math., Phys. Eng. Sci. (2020), https://doi.org/10.1098/rspa.2020.0671.

[78] M.J. Blunt, A. Alhosani, Q. Lin, A. Scanziani, B. Bijeljic, Determination of contact angles for three-phase flow in porous media using an energy balance, J. Colloid Interface Sci. (2021), https://doi.org/10.1016/j.jcis.2020.07.152.

[79] M.J. Sabti, A.H. Alizadeh, M. Piri, In-situ investigation of the impact of spreading on matrix-fracture interactions during three-phase flow in fractured porous media, Adv. Water Resour. (2019), https://doi.org/10.1016/j.advwatres.2019.05.017.

[80] M. Feali et al., Qualitative and quantitative analysis of three-phase distributions of oil, water and gas in Bentheimer sandstone using micro-CT imaging, in *SPE Latin American and Caribbean Petroleum Engineering Conference Proceedings*, 2012. doi: 10.2118/151609-ms.

[81] R. Aziz, V. Joekar-Niasar, P.J. Martínez-Ferrer, O.E. Godinez-Brizuela, C. Theodoropoulos, H. Mahani, Novel insights into pore-scale dynamics of wettability alteration during low salinity waterflooding, Sci. Rep. (2019), https://doi.org/10.1038/s41598-019-45434-2.

[82] W.B. Bartels, et al., Fast X-ray micro-CT study of the impact of brine salinity on the pore-scale fluid distribution during waterflooding, *Petrophysics* (2017).

[83] W.B. Bartels, H. Mahani, S. Berg, S.M. Hassanizadeh, Literature review of low salinity waterflooding from a length and time scale perspective, Fuel (2019), https://doi.org/10.1016/j.fuel.2018.09.018.

[84] A. Selem, N. Agenet, Y. Gao, Q. Lin, M.J. Blunt, and B. Bijeljic, Pore-Scale Imaging of Controlled-Salinity Waterflooding in a Heterogeneous Carbonate Rock at Reservoir Conditions, 2021. doi: 10.3997/2214–4609.202011795.

[85] P. Gouze, L. Luquot, X-ray microtomography characterization of porosity, permeability and reactive surface changes during dissolution, J. Contam. Hydrol. vol. 120–121 (. 2011) 45–55, https://doi.org/10.1016/J.JCONHYD.2010.07.004.

[86] H. Yasuhara, A. Polak, Y. Mitani, A.S. Grader, P.M. Halleck, D. Elsworth, Evolution of fracture permeability through fluid–rock reaction under hydrothermal conditions, Earth Planet Sci. Lett. vol. 244 (1–2) (. 2006) 186–200, https://doi.org/10.1016/J.EPSL.2006.01.046.

[87] M.N. Rad, N. Shokri, A. Keshmiri, P.J. Withers, Effects of grain and pore size on salt precipitation during evaporation from porous media, Transp. Porous Media vol. 110 (2) (2015) 281–294, https://doi.org/10.1007/s11242-015-0515-8.

[88] C. Chen, A.I. Packman, J.F. Gaillard, Pore-scale analysis of permeability reduction resulting from colloid deposition, Geophys Res Lett. (2008), https://doi.org/10.1029/2007GL033077.

[89] G. Mikolajczyk, L. Huang, M. Wilhelm, W. Dreher, S. Odenbach, Colloid deposition in monolithic porous media – experimental investigations using X-ray computed microtomography and magnetic resonance velocimetry, Chem. Eng. Sci. (2018), https://doi.org/10.1016/j.ces.2017.09.054.

[90] X. Li, C.L. Lin, I.D. Miller, W.P. Johnson, Pore-scale observation of microsphere deposition at grain-to-grain contacts over assemblage-scale porous media domains using x-ray microtomography, Environ. Sci. Technol. (2006), https://doi.org/10.1021/es0525004.

[91] D. Soto-Gómez, P. Pérez-Rodríguez, L. Vázquez Juíz, J.E. López-Periago, M. Paradelo Pérez, A new method to trace colloid transport pathways in macroporous soils using X-ray computed tomography and fluorescence macrophotography, Eur. J. Soil Sci. (2019), https://doi.org/10.1111/ejss.12783.

[92] T. Pak, N.L. Archilha, I.F. Mantovani, A.C. Moreira, I.B. Butler, The dynamics of nanoparticle-enhanced fluid displacement in porous media - a pore-scale study, Sci. Rep. vol. 8 (1) (2018), 11148, https://doi.org/10.1038/s41598-018-29569-2.

[93] T. Pak, N.L. Archilha, I.F. Mantovani, A.C. Moreira, C.P. Fernandes, and I. Butler, Nanoparticle-enhanced immiscible fluid displacement in porous rocks, 9th International Conference on Porous Media & Annual Meeting, 2017.

[94] J.P. Owejan, J.J. Gagliardo, J.M. Sergi, S.G. Kandlikar, T.A. Trabold, Water management studies in PEM fuel cells, Part I: fuel cell design and in situ water distributions, Int J. Hydrog. Energy (2009), https://doi.org/10.1016/j.ijhydene.2008.12.100.

[95] T. Doerenkamp, M. Sabharwal, J. Eller, Insights into the stability and formation of water droplets using operando X-ray tomographic microscopy, ECS Meet. Abstr. vol. MA2021–02 (36) (2021), https://doi.org/10.1149/ma2021-02361026mtgabs.

[96] R. Alink, D. Gerteisen, W. Mérida, Investigating the water transport in porous media for PEMFCs by liquid water visualization in ESEM, *Fuel Cells* (2011), https://doi.org/10.1002/fuce.201000110.

[97] J.H. Nam, M. Kaviany, Effective diffusivity and water-saturation distribution in single- and two-layer PEMFC diffusion medium, Int J. Heat. Mass Transf. (2003), https://doi.org/10.1016/S0017-9310(03)00305-3.

[98] S. Litster, D. Sinton, N. Djilali, Ex situ visualization of liquid water transport in PEM fuel cell gas diffusion layers, J. Power Sources (2006), https://doi.org/10.1016/j.jpowsour.2005.03.199.

[99] H.M. Yu, J.O. Schumacher, M. Zobel, C. Hebling, Analysis of membrane electrode assembly (MEA) by environmental scanning electron microscope (ESEM), J. Power Sources (2005), https://doi.org/10.1016/j.jpowsour.2004.12.069.

[100] J.H. Nam, K.J. Lee, G.S. Hwang, C.J. Kim, M. Kaviany, Microporous layer for water morphology control in PEMFC, Int J. Heat. Mass Transf. (2009), https://doi.org/10.1016/j.ijheatmasstransfer.2009.01.002.

[101] A. Mohseninia, et al., Enhanced water management in PEMFCs: perforated catalyst layer and microporous layers, ChemSusChem (2020), https://doi.org/10.1002/cssc.202000542.

[102] P. Shrestha, C.H. Lee, K.F. Fahy, M. Balakrishnan, N. Ge, A. Bazylak, Formation of liquid water pathways in PEM fuel cells: a 3-D pore-scale perspective, J. Electrochem Soc. (2020), https://doi.org/10.1149/1945-7111/ab7a0b.

[103] H.-R. (Molly) Jhong, F.R. Brushett, L. Yin, D.M. Stevenson, P.J.A. Kenis, Combining structural and electrochemical analysis of electrodes using micro-computed tomography and a microfluidic fuel cell, J. Electrochem Soc. (2012), https://doi.org/10.1149/2.033203jes.

[104] J. Eller, J. Roth, F. Marone, M. Stampanoni, F.N. Büchi, Operando properties of gas diffusion layers: saturation and liquid permeability, J. Electrochem Soc. (2017), https://doi.org/10.1149/2.0881702jes.

[105] I. Manke, et al., Investigation of water evolution and transport in fuel cells with high resolution synchrotron x-ray radiography, Appl. Phys. Lett. vol. 90 (17) (2007), https://doi.org/10.1063/1.2731440.

[106] H.W. Shafaque, et al., Boosting membrane hydration for high current densities in membrane electrode assembly CO2Electrolysis, ACS Appl. Mater. Interfaces vol. 12 (49) (2020), https://doi.org/10.1021/acsami.0c14832.

[107] A. Bazylak, Liquid water visualization in PEM fuel cells: a review, Int. J. Hydrog. Energy (2009), https://doi.org/10.1016/j.ijhydene.2009.02.084.

[108] M. Jouny, W. Luc, F. Jiao, General techno-economic analysis of CO_2 electrolysis systems, Ind. Eng. Chem. Res (2018), https://doi.org/10.1021/acs.iecr.7b03514.

[109] F.P. García de Arquer, et al., CO_2 electrolysis to multicarbon products at activities greater than 1 A cm−2, Science 1979 (2020), https://doi.org/10.1126/science.aay4217.

[110] T. Burdyny, W.A. Smith, CO_2 reduction on gas-diffusion electrodes and why catalytic performance must be assessed at commercially-relevant conditions, Energy Environ. Sci. (2019), https://doi.org/10.1039/c8ee03134g.

[111] H.W. Shafaque, et al., Boosting membrane hydration for high current densities in membrane electrode assembly CO 2 electrolysis, ACS Appl. Mater. Interfaces (2020), https://doi.org/10.1021/acsami.0c14832.

[112] C.H. Lee, B. Zhao, J.K. Lee, K.F. Fahy, K. Krause, A. Bazylak, Bubble formation in the electrolyte triggers voltage instability in CO_2 electrolyzers, iScience (2020), https://doi.org/10.1016/j.isci.2020.101094.

[113] D.T. Whipple, P.J.A. Kenis, Prospects of CO_2 utilization via direct heterogeneous electrochemical reduction, J. Phys. Chem. Lett. (2010), https://doi.org/10.1021/jz1012627.

[114] J. Le Houx, D. Kramer, X-ray tomography for lithium ion battery electrode characterisation — a review, Energy Rep. vol. 7 (2021) 9–14, https://doi.org/10.1016/J.EGYR.2021.02.063.

[115] R. Franke-Lang, T. Arlt, I. Manke, J. Kowal, X-ray tomography as a powerful method for zinc-air battery research, J. Power Sources vol. 370 (. 2017) 45–51, https://doi.org/10.1016/J.JPOWSOUR.2017.10.010.

[116] J. Scharf, et al., Bridging nano- and microscale X-ray tomography for battery research by leveraging artificial intelligence, *2022 17:5*, Nat. Nanotechnol. vol. 17 (5) (2022) 446–459, https://doi.org/10.1038/s41565-022-01081-9.

[117] P. Pietsch and V. Wood, X-Ray Tomography for Lithium Ion Battery Research: A Practical Guide, https://doi.org/10.1146/annurev-matsci-070616–123957, vol. 47, pp. 451–479, Jul. 2017, doi: 10.1146/ANNUREV-MATSCI-070616–123957.

[118] V. Wood, X-ray tomography for battery research and development, *2018 3:9*, Nat. Rev. Mater. vol. 3 (9) (2018) 293–295, https://doi.org/10.1038/s41578-018-0053-4.

[119] E. Unsal, M. Rücker, S. Berg, W.B. Bartels, A. Bonnin, Imaging of compositional gradients during in situ emulsification using X-ray micro-tomography, J. Colloid Interface Sci. (2019), https://doi.org/10.1016/j.jcis.2019.04.068.

[120] Y. Wang, S. Jia, M. Wei, L. Peng, Y. Wu, X. Liu, Research progress on solidification structure of alloys by synchrotron X-ray radiography: A review, J. Magnes. Alloy. (2020), https://doi.org/10.1016/j.jma.2019.08.003.

[121] K.M. Kareh, P.D. Lee, R.C. Atwood, T. Connolley, C.M. Gourlay, Revealing the micromechanisms behind semi-solid metal deformation with time-resolved X-ray tomography, Nat. Commun. (2014), https://doi.org/10.1038/ncomms5464.

[122] P. Jarry, M. Rappaz, Recent advances in the metallurgy of aluminium alloys. Part I: solidification and casting, Comptes Rendus Phys. (2018), https://doi.org/10.1016/j.crhy.2018.09.003.

[123] A.J. Clarke, et al., X-ray imaging and controlled solidification of Al-Cu alloys toward microstructures by design, Adv. Eng. Mater. (2015), https://doi.org/10.1002/adem.201400469.

[124] Y. Zhang, W. Verwaal, M.F.C. van de Ven, A.A.A. Molenaar, S.P. Wu, Using high-resolution industrial CT scan to detect the distribution of rejuvenation products in porous asphalt concrete, Constr. Build. Mater. vol. 100 (. 2015) 1–10, https://doi.org/10.1016/J.CONBUILDMAT.2015.09.064.

[125] J. Wang, J. Dewanckele, V. Cnudde, S. Van Vlierberghe, W. Verstraete, N. De Belie, X-ray computed tomography proof of bacterial-based self-healing in concrete, Cem. Concr. Compos vol. 53 (. 2014) 289–304, https://doi.org/10.1016/J.CEMCONCOMP.2014.07.014.

[126] C. Sun, J. McClure, S. Berg, P. Mostaghimi, R.T. Armstrong, Universal description of wetting on multiscale surfaces using integral geometry, J. Colloid Interface Sci. vol. 608 (2022), https://doi.org/10.1016/j.jcis.2021.10.152.

[127] Q. Lin, B. Bijeljic, S. Berg, R. Pini, M.J. Blunt, S. Krevor, Minimal surfaces in porous media: pore-scale imaging of multiphase flow in an altered-wettability Bentheimer sandstone, Phys. Rev. E vol. 99 (6) (2019), https://doi.org/10.1103/PhysRevE.99.063105.

[128] M.C. Tan, N.L. Chin, Y.A. Yusof, J. Abdullah, Novel 2D and 3D imaging of internal aerated structure of ultrasonically treated foams and cakes using X-ray tomography and X-ray microtomography, J. Food Eng. (2016), https://doi.org/10.1016/j.jfoodeng.2016.03.008.

[129] R. Kobayashi, N. Kimizuka, M. Watanabe, T. Suzuki, The effect of supercooling on ice structure in tuna meat observed by using X-ray computed tomography, Int. J. Refrig. (2015), https://doi.org/10.1016/j.ijrefrig.2015.07.011.

[130] M.S. Costanza-Robinson, B.D. Estabrook, D.F. Fouhey, Representative elementary volume estimation for porosity, moisture saturation, and air-water interfacial areas in unsaturated porous media: data quality implications, Water Resour. Res vol. 47 (7) (2011), https://doi.org/10.1029/2010WR009655.

[131] S.J. Jackson, Q. Lin, S. Krevor, Representative elementary volumes, hysteresis, and heterogeneity in multiphase flow from the pore to continuum scale, Water Resour. Res vol. 56 (6) (2020), https://doi.org/10.1029/2019WR026396.

[132] R. Huang, A.L. Herring, A. Sheppard, Effect of saturation and image resolution on representative elementary volume and topological quantification: an experimental study on bentheimer sandstone using micro-CT, Transp. Porous Media vol. 137 (3) (2021), https://doi.org/10.1007/s11242-021-01571-9.

[133] Jacob. Bear, Dynamics of fluids in porous media, American Elsevier Pub. Co, 1972.

[134] T. Pak, I.B. Butler, S. Geiger, M.I.J. van Dijke, Z. Jiang, R. Surmas, Multiscale pore-network representation of heterogeneous carbonate rocks, Water Resour. Res vol. 52 (7) (. 2016) 5433–5441, https://doi.org/10.1002/2016WR018719.

[135] C. Zahasky, S.J. Jackson, Q. Lin, S. Krevor, Pore network model predictions of darcy-scale multiphase flow heterogeneity validated by experiments, Water Resour. Res vol. 56 (6) (2020), https://doi.org/10.1029/2019WR026708.

[136] S. Manoorkar, S.J. Jackson, S. Krevor, Observations of the impacts of millimeter-to centimeter-scale heterogeneities on relative permeability and trapping in carbonate rocks, p. e2020WR028597, Water Resour. Res vol. 57 (4) (. 2021), https://doi.org/10.1029/2020WR028597.

[137] W.B. Bartels, et al., Imaging spontaneous imbibition in full darcy-scale samples at pore-scale resolution by fast X-ray tomography, Water Resour. Res vol. 55 (8) (. 2019) 7072–7085, https://doi.org/10.1029/2018WR024541.

[138] L. Gerward, N. Guilbert, K. Bjørn Jensen, H. Levring, X-ray absorption in matter. Reengineering XCOM, Radiat. Phys. Chem. vol. 60 (1–2) (. 2001) 23–24, https://doi.org/10.1016/S0969-806X(00)00324-8.

[139] R.D. Hanna, R.A. Ketcham, X-ray computed tomography of planetary materials: a primer and review of recent studies, Chem. der Erde vol. 77 (4) (2017), https://doi.org/10.1016/j.chemer.2017.01.006.

[140] Matweb, MatWeb, Material property data, MatWeb, pp. 1–2, 2015, [Online]. Available: http://www.matweb.com/search/datasheet.aspx?MatGUID=ff6d4e6d529e4b3d97c77d6538b29693

[141] ASM Handbook Committee, Properties and Selection: Nonferrous Alloys and Special-Purpose Materials: Properties of Wrought Aluminum and Aluminum Alloys, ASM Handbook, vol. Volume 2, 1990.

[142] M.A. Khan, et al., Effect of heat treatment on the precipitate behaviour, corrosion resistance and high temperature tensile properties of 7055 aluminum alloy synthesis by novel spray deposited followed by hot extrusion, Vacuum vol. 174 (2020), https://doi.org/10.1016/j.vacuum.2020.109185.

[143] I. Butler, F. Fusseis, A. Cartwright-Taylor, M. Flynn, Mjölnir: a miniature triaxial rock deformation apparatus for 4D synchrotron X-ray microtomography, J. Synchrotron Radiat. vol. 27 (6) (. 2020) 1681–1687, https://doi.org/10.1107/S160057752001173X/PP5161SUP2.PDF.

[144] J.R. Ferreira, N.L. Coppini, G.W.A. Miranda, Machining optimisation in carbon fibre reinforced composite materials, J. Mater. Process Technol. vol. 92–93 (. 1999) 135–140, https://doi.org/10.1016/S0924-0136(99)00221-6.

[145] E. Publications, SCOEL/REC/175 beryllium and inorganic beryllium compounds - EU Law and Publications. doi: 10.2767/72169.

[146] Q. Lin, B. Bijeljic, H. Rieke, M.J. Blunt, Visualization and quantification of capillary drainage in the pore space of laminated sandstone by a porous plate method using differential imaging X-ray microtomography, Water Resour. Res vol. 53 (8) (2017), https://doi.org/10.1002/2017WR021083.

[147] F.A.L. Dullien, Porous media: fluid transport and pore structure 2nd ed. (p.), Academic Press, *San Diego, CA*, 1992, p. 574.

[148] M. Rcker et al., The Fate of Oil Clusters During Fractional Flow: Trajectories in the Saturation - Capillary Number Space, in *International Symposium of the Society of Core Analysts*, Canada, 2015.

[149] R.T. Armstrong, H. Ott, A. Georgiadis, M. Rücker, A. Schwing, S. Berg, Subsecond pore-scale displacement processes and relaxation dynamics in multiphase flow, Water Resour. Res vol. 50 (12) (2014) 9162–9176, https://doi.org/10.1002/2014WR015858.

[150] T. De Schryver, et al., Motion compensated micro-CT reconstruction for in-situ analysis of dynamic processes, Sci. Rep. vol. 8 (1) (2018), https://doi.org/10.1038/s41598-018-25916-5.

[151] A.M. Kingston, G.R. Myers, S.J. Latham, B. Recur, H. Li, A.P. Sheppard, Space-filling X-ray source trajectories for efficient scanning in large-angle cone-beam computed tomography, IEEE Trans. Comput. Imaging vol. 4 (3) (2018) 447–458, https://doi.org/10.1109/TCI.2018.2841202.

[152] G.R. Myers, M. Geleta, A.M. Kingston, B. Recur, A.P. Sheppard, Improving dynamic tomography, through maximum a posteriori estimation, Proc. SPIE - Int. Soc. Opt. Eng. vol. 9212 (Ml) (2014), 921211, https://doi.org/10.1117/12.2061604.

[153] T. Bultreys, et al., Fast laboratory-based micro-computed tomography for pore-scale research: Illustrative experiments and perspectives on the future, Adv. Water Resour. vol. 95 (. 2016) 341–351, https://doi.org/10.1016/J.ADVWATRES.2015.05.012.

[154] R. Mokso, et al., GigaFRoST: the gigabit fast readout system for tomography, J. Synchrotron Radiat. vol. 24 (6) (. 2017) 1250–1259, https://doi.org/10.1107/S1600577517013522.

[155] F. Renard, et al., A deformation rig for synchrotron microtomography studies of geomaterials under conditions down to 10km depth in the Earth, J. Synchrotron Radiat. vol. 23 (4) (. 2016) 1030–1034, https://doi.org/10.1107/S1600577516008730.

[156] D.D. Huang, M.M. Honarpour, Capillary end effects in coreflood calculations, J. Pet. Sci. Eng. vol. 19 (1–2) (1998), https://doi.org/10.1016/S0920-4105(97)00040-5.

[157] S. Berg, E. Unsal, H. Dijk, Non-uniqueness and uncertainty quantification of relative permeability measurements by inverse modelling, Comput. Geotech. vol. 132 (2021), https://doi.org/10.1016/j.compgeo.2020.103964.

[158] T.G. Sorop et al., Relative Permeability Measurements to Quantify the Low Salinity Flooding Effect at Field Scale, Society of Petroleum Engineers - Abu Dhabi International Petroleum Exhibition and Conference, ADIPEC *2015*, Nov. 2015, doi: 10.2118/177856-MS.

[159] S.K. Masalmeh et al., Low salinity flooding: Experimental evaluation and numerical interpretation, Society of Petroleum Engineers - International Petroleum Technology Conference 2014, IPTC 2014: Unlocking Energy Through Innovation, Technology and Capability, vol. 4, pp. 2910–2922, Jan. 2014, doi: 10.3997/2214–4609-PDB.395.IPTC-17558-MS/CITE/REFWORKS.

[160] S. Berg, E. Unsal, H. Dijk, Sensitivity and uncertainty analysis for parameterization of multiphase flow models, Transp. Porous Media vol. 140 (1) (2021), https://doi.org/10.1007/s11242-021-01576-4.

[161] D.E. Meisenheimer, M.L. Rivers, D. Wildenschild, Optimizing pink-beam fast X-ray microtomography for multiphase flow in 3D porous media, J. Microsc. vol. 277 (2) (. 2020) 100–106, https://doi.org/10.1111/JMI.12872.

[162] B. Bazin, M.T. Bieber, C. Roque, and M. Bouteca, Improvement in the Characterization of the Acid Wormholing by "In Situ" X-Ray CT Visualizations, in SPE Formation Damage Control Symposium, Society of Petroleum Engineers, Apr. 1996. doi: 10.2118/31073-MS.

[163] M.E. Coles, R.D. Hazlett, P. Spanne, W.E. Soll, E.L. Muegge, K.W. Jones, Pore level imaging of fluid transport using synchrotron X-ray microtomography, J. Pet. Sci. Eng. vol. 19 (1–2) (1998) 55–63, https://doi.org/10.1016/S0920-4105(97)00035-1.

[164] J.M. Schembre, A.R. Kovscek, A technique for measuring two-phase relative permeability in porous media via X-ray CT measurements, J. Pet. Sci. Eng. vol. 39 (1–2) (. 2003) 159–174, https://doi.org/10.1016/S0920-4105(03)00046-9.

[165] G. Viggiani, et al., X-ray microtomography for studying localized deformation in fine-grained geomaterials under triaxial compression, Comptes Rendus Mécanique vol. 332 (10) (2004) 819–826, https://doi.org/10.1016/j.crme.2004.05.006.

[166] G. Schnaar, M.L. Brusseau, Pore-scale characterization of organic immiscible-liquid morphology in natural porous media using synchrotron x-ray microtomography, Environ. Sci. Technol. vol. 39 (21) (2005) 8403–8410, https://doi.org/10.1021/es0508370.

[167] F. Fusseis, et al., A low-cost X-ray-transparent experimental cell for synchrotron-based X-ray microtomography studies under geological reservoir conditions, J. Synchrotron Radiat. vol. 21 (1) (. 2014) 251–253, https://doi.org/10.1107/S1600577513026969.

[168] M. Lebedev, S. Iglauer, V. Mikhaltsevich, Acoustic response of reservoir sandstones during injection of supercritical CO_2, Energy Procedia vol. 63 (. 2014) 4281–4288, https://doi.org/10.1016/J.EGYPRO.2014.11.463.

[169] N. Tisato, Q. Zhao, A. Biryukov, and G. Grasselli, Experimental Rock Deformation under micro-CT: ERDμ, in EGU General Assembly 2015, held 12–17 April, 2015 in Vienna, Austria. id.3590, 2015.

[170] K.J. Dobson, S.B. Coban, S.A. McDonald, J.N. Walsh, R.C. Atwood, P.J. Withers, 4-D imaging of sub-second dynamics in pore-scale processes using real-time synchrotron X-ray tomography, Solid Earth vol. 7 (4) (2016) 1059–1073, https://doi.org/10.5194/se-7-1059-2016.

[171] R. Jervis, et al., Design of a miniature flow cell for in situ x-ray imaging of redox flow batteries, J. Phys. D. Appl. Phys. vol. 49 (43) (. 2016), 434002, https://doi.org/10.1088/0022-3727/49/43/434002.
[172] L.E. Dalton, K.A. Klise, S. Fuchs, D. Crandall, A. Goodman, Methods to measure contact angles in scCO2-brine-sandstone systems, Adv. Water Resour. vol. 122 (2018), https://doi.org/10.1016/j.advwatres.2018.10.020.
[173] P.E. Øren, L.C. Ruspini, M. Saadatfar, R.M. Sok, M. Knackstedt, A. Herring, In-situ pore-scale imaging and image-based modelling of capillary trapping for geological storage of CO_2, Int. J. Greenh. Gas. Control vol. 87 (2019), https://doi.org/10.1016/j.ijggc.2019.04.017.
[174] S. Berg, et al., Determination of critical gas saturation by micro-CT, in, Petrophysics (2020), https://doi.org/10.30632/PJV61N2-2020al.
[175] N.S. Lenchenkov, M. Slob, G. Glasbergen, C. van Kruijsdijk, Propagation of polymer nanospheres in outcrop cores, SPE J. vol. 24 (6) (2019), https://doi.org/10.2118/194489-PA.
[176] S. Berg, et al., Miscible displacement of oils by carbon disulfide in porous media: experiments and analysis, Phys. Fluids vol. 22 (11) (2010), https://doi.org/10.1063/1.3516614.
[177] F.P. Beer, R. Johnston, J. Dewolf, D. Mazurek, Mechanics of Materials, McGraw-Hill, 2013.
[178] R.G. Budynas, J.K. Nisbett, Shigley's mechanical engineering design, nineth ed., McGraw-Hill, 2017.
[179] A. Jahanbakhsh, K.L. Wlodarczyk, D.P. Hand, R.R.J. Maier, M.M. Maroto-Valer, Review of microfluidic devices and imaging techniques for fluid flow study in porous geomaterials, Sensors vol. 20 (14) (2020), https://doi.org/10.3390/s20144030.
[180] I.M. Zarikos, S.M. Hassanizadeh, L.M. van Oosterhout, W. van Oordt, Manufacturing a micro-model with integrated fibre optic pressure sensors, Transp. Porous Media vol. 122 (1) (2018), https://doi.org/10.1007/s11242-018-1000-y.
[181] E.V. Lebedeva, A. Fogden, Micro-CT and wettability analysis of oil recovery from sand packs and the effect of waterflood salinity and kaolinite, Energy Fuels vol. 25 (12) (2011), https://doi.org/10.1021/ef201242s.